

Extreme multiplicity in cylindrical Rayleigh-Bénard convection: II. Bifurcation diagram and symmetry classification

Katarzyna Borońska^{1,*} and Laurette S. Tuckerman^{2,†}

¹*School of Computing, University of Leeds, Leeds LS2 9JT, United Kingdom*

²*PMMH-ESPCI, CNRS (UMR7636), Univ. Paris VI & VII, 10 rue Vauquelin, 75231 Paris France*

(Dated: May 29, 2018)

A large number of flows with distinctive patterns have been observed in experiments and simulations of Rayleigh-Bénard convection in a water-filled cylinder whose radius is twice the height. We have adapted a time-dependent pseudospectral code, first, to carry out Newton's method and branch continuation and, second, to carry out the exponential power method and Arnoldi iteration to calculate leading eigenpairs and determine the stability of the steady states. The resulting bifurcation diagram represents a compromise between the tendency in the bulk towards parallel rolls, and the requirement imposed by the boundary conditions that primary bifurcations be towards states whose azimuthal dependence is trigonometric. The diagram contains 17 branches of stable and unstable steady states. These can be classified geometrically as roll states containing two, three, and four rolls; axisymmetric patterns with one or two tori; three-fold symmetric patterns called mercedes, mitubishi, marigold and cloverleaf; trigonometric patterns called dipole and pizza; and less symmetric patterns called CO and asymmetric three-rolls. The convective branches are connected to the conductive state and to each other by 16 primary and secondary pitchfork bifurcations and turning points. In order to better understand this complicated bifurcation diagram, we have partitioned it according to azimuthal symmetry. We have been able to determine the bifurcation-theoretic origin from the conductive state of all the branches observed at high Rayleigh number.

PACS numbers: 47.20.Ky, 47.20.Bp, 47.10.Fg, 47.11.Kb

I. INTRODUCTION

In the late 1990s, Hof, Lucas and Mullin [1, 2] described five distinct steady patterns observed experimentally in a cylindrical Rayleigh-Bénard convection cell at identical parameter values. More precisely, the patterns observed were torus, two-, three-, and four-roll states, and a mercedes pattern, at Prandtl number $Pr = 6.7$, Rayleigh number $Ra = 14\,200$, and an aspect ratio $\Gamma \equiv \text{radius}/\text{height} = 2$ with insulating lateral boundaries. In our previous work [3, 4], we reproduced numerically the five patterns observed by Hof and determined the approximate limits in Rayleigh number over which they could be observed. At lower Rayleigh numbers, we simulated several other patterns – dipole, pizza, and two-tori – as well as some time-periodic patterns. These results are summarized in figure 1. Our viewpoint, pioneered in the 1980s by Benjamin and Mullin [5], is that these observations can be best understood and organized by constructing the bifurcation diagram corresponding to this figure. In particular, we wish to trace connections between the patterns observed at high and at low Rayleigh numbers, and to the basic conductive state wherever possible.

The classical analysis of onset of Rayleigh-Bénard convection describes an instability of the conductive state to a pattern of straight parallel rolls of infinite length. However, such a pattern is clearly not realizable in a small-aspect-ratio cylinder. Rolls must be curved to fit into the container, as shown in the two-, three- and four-roll states illustrated in figure 1. In addition, a primary bifurcation, that is, a bifurcation from the conductive state, is associated with an eigenmode which is necessarily trigonometric in the azimuthal angle, such as the dipole or pizza states, or two-tori and torus states of figure 1. The focus of this paper is the relationship between trigonometric modes and roll states and, more generally, the bifurcation-theoretic genesis of the profusion of states in this configuration.

In our companion paper [4], we reviewed some of the literature on Rayleigh-Bénard convection in small-aspect-ratio cylindrical geometries, focusing on pattern competition. The previous investigations most relevant to this manuscript, in addition to those of Hof et al. [1, 2], are the full nonlinear simulations of Leong [6] and of Ma *et al.* [7]; we will compare our results to these articles where appropriate.

In section II we state the governing equations and the symmetries of the configuration. Section III describes the numerical methods we have used to compute steady states and their stability. Section IV begins by presenting the

*k.boronska@leeds.ac.uk; www.comp.leeds.ac.uk/kb

†laurette@pmmh.espci.fr; www.pmmh.espci.fr/~laurette

full bifurcation diagram and primary bifurcations. We then give a detailed analysis of branches corresponding to each azimuthal wavenumber. Concluding remarks are presented in section V.

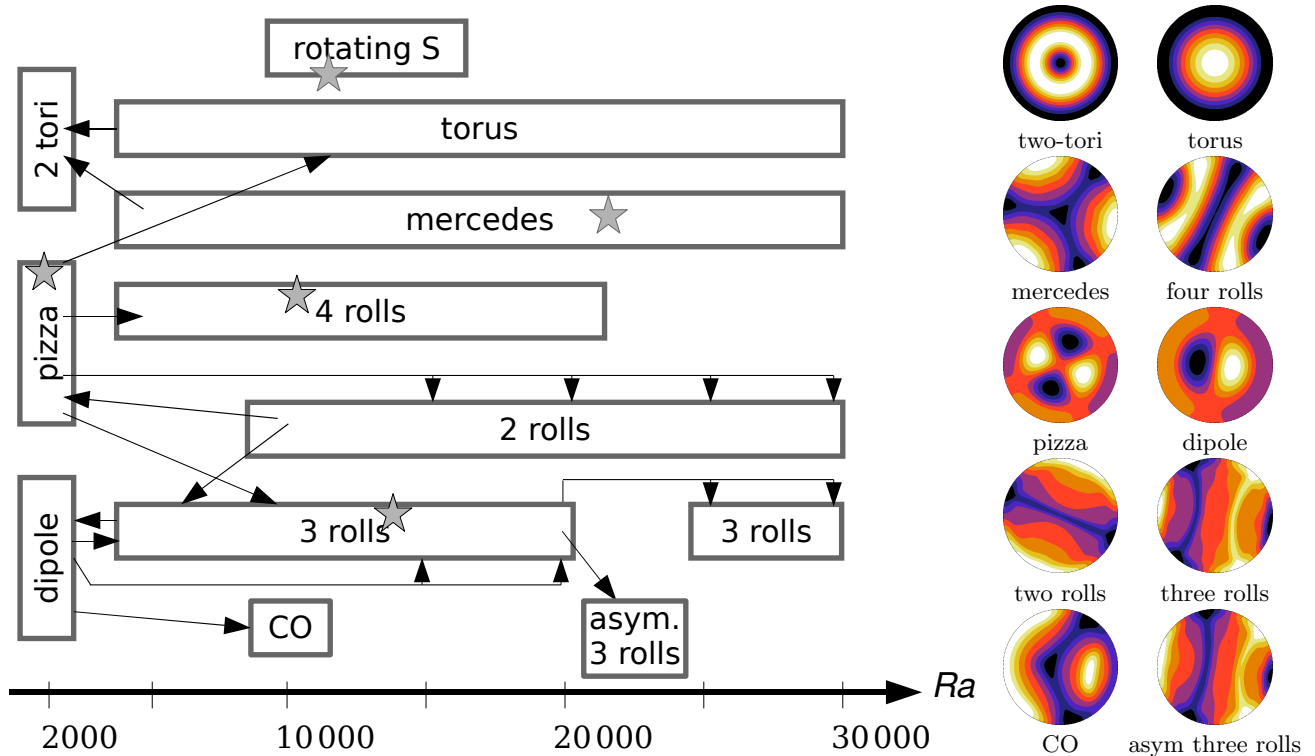


FIG. 1: (Color online) Schematic diagram of existence ranges and transitions between convective patterns observed in time-dependent simulation for insulating sidewalls. Stars denote solutions obtained from a slight perturbation of the conductive state, at the Rayleigh numbers indicated. The initial condition was identical for all five simulations. Arrows indicate patterns obtained by starting from stable steady states, and abruptly either lowering or raising the Rayleigh number. For example, at $Ra = 2000$, the perturbed conductive initial condition leads to a pizza state. Using the pizza state at $Ra = 2000$ as an initial condition leads to a four-roll state at $Ra = 5000$, to the three-roll state at $Ra = 10000$, and to a two-roll state at $Ra \geq 15000$. Right: representative patterns illustrated via temperature field in the horizontal midplane, with light portions representing hot rising fluid and dark portions representing cold descending fluid.

II. BACKGROUND

A. Governing equations and boundary conditions

We recall from our companion paper [4] the dimensionless Navier–Stokes and Boussinesq equations governing the system:

$$\partial_t H + (\mathbf{U} \cdot \nabla) H = Ra U_z + \nabla^2 H, \quad (1a)$$

$$Pr^{-1} (\partial_t \mathbf{U} + (\mathbf{U} \cdot \nabla) \mathbf{U}) = -\nabla P + \nabla^2 \mathbf{U} + H \mathbf{e}_z, \quad (1b)$$

$$\nabla \cdot \mathbf{U} = 0, \quad (1c)$$

where H is the nondimensionalized deviation of the temperature from the linear vertical conductive profile. The parameter values are as follows:

$$Pr = 6.7, \quad \Gamma \equiv \frac{\text{radius}}{\text{height}} = 2, \quad 0 \leq Ra \leq 30000. \quad (2)$$

The container is assumed to have rigid walls, with thermally conducting horizontal bounding plates and thermally insulating sidewalls

$$\mathbf{U} = 0 \quad \text{for } z = \pm 1/2 \quad \text{or } r = \Gamma, \quad (3a)$$

$$H = 0 \quad \text{for } z = \pm 1/2, \quad (3b)$$

$$\partial_r H = 0 \quad \text{for } r = \Gamma \quad (3c)$$

B. Symmetries

The bifurcations that this system can undergo are dictated by its symmetries. In group-theoretic terms, the conductive state has $O(2)$ symmetry in the azimuthal angle, meaning that it is invariant under all rotations and reflections in θ :

$$(U_r, U_\theta, U_z, H)(r, \theta, z) = (U_r, U_\theta, U_z, H)(r, \theta + \theta_0, z) \quad (4a)$$

$$(U_r, U_\theta, U_z, H)(r, \theta, z) = (U_r, -U_\theta, U_z, H)(r, \theta_0 - \theta, z) \quad (4b)$$

where θ_0 indicates an arbitrary angle of rotation or axis of reflection, and all compositions of these transformations. Under the Boussinesq approximation, the conductive state is also invariant under simultaneous reflection in z and change in sign of the temperature perturbation:

$$(U_r, U_\theta, U_z, H)(r, \theta, z) = (U_r, U_\theta, -U_z, -H)(r, \theta, -z)$$

This symmetry can be combined with the θ -rotation symmetry (4a) to yield:

$$(U_r, U_\theta, U_z, H)(r, \theta, z) = (U_r, U_\theta, -U_z, -H)(r, \theta + \theta_0, -z) \quad (4c)$$

a form whose utility will appear shortly. The full symmetry group of the conductive state is thus $O(2) \times Z_2$.

A steady bifurcation from the axisymmetric conductive state, i.e. a primary bifurcation, is necessarily associated with an eigenvector which is trigonometric in the azimuthal direction; see, e.g. Crawford & Knobloch [14]. Each bifurcating branch is thus associated with an azimuthal wavenumber m . For $m = 0$, symmetry (4c) is broken and the bifurcation is a pitchfork, leading to two branches. If m is non-zero, the bifurcation is a circle pitchfork, producing families of states of arbitrary orientation. For the bifurcating states, $O(2)$ symmetry is replaced by D_m , meaning that they are invariant under rotation by angles which are multiples of $2\pi/m$ and reflections in $2m$ axes of symmetry:

$$(U_r, U_\theta, U_z, H)(r, \theta, z) = (U_r, U_\theta, U_z, H)(r, \theta + 2\pi/m, z) \quad (5a)$$

$$(U_r, U_\theta, U_z, H)(r, \theta, z) = (U_r, -U_\theta, U_z, H)(r, -\theta, z) \quad (5b)$$

$$(U_r, U_\theta, U_z, H)(r, \theta, z) = (U_r, U_\theta, -U_z, -H)(r, \theta + \pi/m, -z) \quad (5c)$$

where $\theta = 0$ is taken to be one of the axes of symmetry of the pattern, and (5a) is trivially verified if $m = 1$. These equations generate the symmetry group $D_m \times Z_2$. These states have a zero eigenvalue, corresponding to the marginal stability to rotation of the pattern. Equations (5) can be seen to be special cases of (4). (The form of (5c) is the reason we choose (4c), instead of the Boussinesq reflection operator, as a generator of the symmetry group.)

Primary branches can undergo secondary pitchfork bifurcations which break the Z_2 symmetry (5c). The resulting branches, which we will call ‘‘asymmetric’’, nonetheless have D_m symmetry, generated by the discrete rotation symmetry (5a) and the reflection symmetry (5b).

III. NUMERICAL METHODS

In [3, 4] we described our code for integrating the time-dependent Boussinesq equations in a cylindrical geometry. We have modified this time-dependent code using the techniques described in [8, 9] to carry out continuation by Newton’s method and linear stability analysis by the exponential Arnoldi method. We describe these modifications in the subsections which follow. To do so, we will write the Boussinesq equations schematically as

$$\frac{d\mathcal{U}}{dt} = \mathcal{L}\mathcal{U} + \mathcal{N}(\mathcal{U}) \quad (6)$$

where \mathcal{L} represents the viscous, diffusive and buoyancy operators and \mathcal{N} the advective terms. $\mathcal{U} \equiv (H, U_r, U_\theta, U_z)$ represents the spatially discretized temperature deviation H and velocity field $\mathbf{U} = (U_r, U_\theta, U_z)$. The imposition of

boundary conditions and incompressibility are assumed to be included in the representations of \mathcal{L} , \mathcal{N} and \mathcal{U} . Here, we assume that timestepping is carried out via the first-order formula:

$$\mathcal{U}(t + \Delta t) = (I - \Delta t \mathcal{L})^{-1} (I + \Delta t \mathcal{N}) \mathcal{U}(t) \equiv \mathcal{B}(\mathcal{U}(t)) \quad (7)$$

i.e. the terms in \mathcal{L} are treated via the implicit backwards Euler scheme and those in \mathcal{N} by the explicit forwards Euler scheme.

A. Spatial discretization

The code uses a pseudo-spectral spatial discretization, in which H , U_z are approximated as:

$$f(r, \theta, z) = \sum_{m=0}^{N_\theta/2} \sum_{\substack{j \geq m \\ j+m \text{ even}}}^{2N_r-1} \sum_{k=0}^{N_z-1} \hat{f}_{j,m,k} T_j(r/\Gamma) T_k(2z) e^{im\theta} + \text{c.c.} \quad (8)$$

while $j+m$ odd is used for U_r , U_θ . Differentiation is carried out on the spectral representation (8), while multiplications are performed after transforming to a grid, and then transforming the result back to the spectral representation. For the aspect ratio $\Gamma = 2$ investigated here, we use $N_r = 40$ gridpoints or Chebyshev polynomials in the radial direction, $N_\theta = 120$ gridpoints or trigonometric functions in the azimuthal direction and $N_z = 20$ gridpoints or Chebyshev polynomials in the axial direction. Thus the domain is represented by approximately 10^5 gridpoints and each solution by a vector of size 4×10^5 . (We have also checked our resolution for $Ra \geq 20000$ by re-calculating a few of our branches – the mercedes, one-torus, two-roll and asymmetric three-roll branches – with a resolution of $N_r \times N_\theta \times N_z = 60 \times 160 \times 30$.) The boundary conditions are imposed via the tau method, and incompressibility to machine accuracy is insured via an influence matrix technique.

B. Steady state solving

Steady states are found by calculating the roots of $\mathcal{B} - I$, which are the same as those of $\mathcal{N} + \mathcal{L}$ for any value of Δt , as shown by the following calculation:

$$\begin{aligned} (\mathcal{B} - I) &= (I - \Delta t \mathcal{L})^{-1} (I + \Delta t \mathcal{N}) - I \\ &= (I - \Delta t \mathcal{L})^{-1} [(I + \Delta t \mathcal{N}) - (I - \Delta t \mathcal{L})] \\ &= (I - \Delta t \mathcal{L})^{-1} \Delta t (\mathcal{N} + \mathcal{L}). \end{aligned} \quad (9)$$

The roots of $\mathcal{B} - I$ are found by Newton iteration:

$$(\mathcal{B}_{\mathcal{U}} - I) u = (\mathcal{B} - I) \mathcal{U} \quad (10a)$$

$$\mathcal{U} \leftarrow \mathcal{U} - u, \quad (10b)$$

where the linear operator $\mathcal{B}_{\mathcal{U}} - I$ is the Jacobian of $\mathcal{B} - I$ evaluated at \mathcal{U} :

$$(\mathcal{B}_{\mathcal{U}} - I) u = (I - \Delta t \mathcal{L})^{-1} \Delta t (\mathcal{N}_{\mathcal{U}} + \mathcal{L}) u \quad (11)$$

while $\mathcal{U} \equiv (H, \mathbf{U})$ is the current estimate for the steady state and $u \equiv (h, \mathbf{u})$ is an unknown correction to \mathcal{U} . The action $\mathcal{N}_{\mathcal{U}} u$ is obtained from $\mathcal{N}(\mathcal{U})$ merely by carrying out the replacements

$$\mathbf{U} \cdot \nabla H \rightarrow \mathbf{U} \cdot \nabla h + \mathbf{u} \cdot \nabla H \quad (12a)$$

$$\mathbf{U} \cdot \nabla \mathbf{U} \rightarrow \mathbf{U} \cdot \nabla \mathbf{u} + \mathbf{u} \cdot \nabla \mathbf{U} \quad (12b)$$

in the nonlinear terms of (1b)-(1a). Since the boundary conditions (3) are homogeneous, they remain unchanged.

We iterate (10) until $\|(\mathcal{B} - I)\mathcal{U}\|$ is lower than some threshold, which we usually take to be $\epsilon_{\text{Newton}} = 10^{-16}$, or until a maximum number of iterations, which we take to be 10, has been surpassed, meaning that the Newton procedure has failed. We use the norm

$$\|\mathcal{U}\| \equiv \frac{1}{Ra \Delta t} \left(\|H\|_\infty + \frac{1}{Pr} \max(\|U_r\|_\infty, \|U_\theta\|_\infty, \|U_z\|_\infty) \right). \quad (13)$$

The size of the matrix representing the linear operator in (10a) is $(4 \times 10^5) \times (4 \times 10^5)$ and so the system is far too large to be solved directly. Instead we use the BiConjugate Gradient Stabilized algorithm [10], which requires the right-hand-side and a procedure for calculating the action of $\mathcal{B}_{\mathcal{U}} - I$ on a vector u . The right-hand-side of (10a) is shown by (9) to be the difference between $U(t + \Delta t) = B(U(t))$ and $U(t)$, i.e. between two (widely spaced) consecutive timesteps, while the left-hand-side is the difference between $B_U(U(t))$ and $U(t)$, i.e. between two *linearized* timesteps. Conjugate gradient iteration proceeds until

$$\frac{\|(\mathcal{B}_{\mathcal{U}} - I)u - (\mathcal{B} - I)\mathcal{U}\|}{\|(\mathcal{B} - I)\mathcal{U}\|} \leq \epsilon_{\text{BiCGS}} \quad (14)$$

where the threshold ϵ_{BiCGS} is taken between 10^{-8} and 10^{-16} . The reason for finding the roots of $\mathcal{B} - I$ instead of those of $\mathcal{N} + \mathcal{L}$ is that, as shown by equation (9),

$$(\mathcal{B}_{\mathcal{U}} - I) \approx \mathcal{L}^{-1}(\mathcal{N}_{\mathcal{U}} + \mathcal{L}) \quad \text{for } \Delta t \gg 1. \quad (15)$$

This effective preconditioning by \mathcal{L}^{-1} makes $\mathcal{B}_{\mathcal{U}} - I$ far better conditioned than $\mathcal{N}_{\mathcal{U}} + \mathcal{L}$, and greatly accelerates the convergence of BiCGSTAB. Note that $\Delta t \gg 1$ is the limit *opposite* to that used in timestepping. We use Δt ranging between 0.2 and 10 (in contrast to the Δt on the order of 10^{-4} used in temporal integration).

It is the solution of the linear system (10a) which poses the greatest difficulty and which determined the limits of our study. In some regions, convergence of BiCGSTAB required as few as 5 actions of $B_U - I$, with more typical values ranging between 30 and 800. In other regions, 4000 iterations did not suffice (even sometimes far from any bifurcation, where singularity of $\mathcal{B}_{\mathcal{U}} - I$ is to be expected), and continuation of the branch was eventually abandoned.

C. Branch following

In order to calculate a branch of steady states, we carry out Newton iteration (10) repeatedly for different values of Rayleigh number. Generally, in the absence of turning points, one can merely use the converged solution for one Ra to initialize the Newton iteration for a neighboring Ra . This initialization procedure constitutes zero-th order extrapolation. We reduce the increment or decrement ΔRa in Ra if the Newton iteration failed to converge in N^{opt} iterations and increase ΔRa if convergence took place sooner. Specifically, if we have computed solutions $\mathcal{U}^{(1)}$, $\mathcal{U}^{(2)}$ corresponding to $Ra^{(1)}$, $Ra^{(2)}$ in $N^{(1)}$, $N^{(2)}$ Newton iterations, we set

$$\begin{aligned} Ra^{(3)} &= Ra^{(2)} + \Delta Ra = Ra^{(2)} + \alpha(Ra^{(2)} - Ra^{(1)}) \\ \alpha &= \frac{N^{\text{opt}} + 1}{N^{(2)} + 1} \end{aligned} \quad (16)$$

where we take N^{opt} between 2 and 5.

Linear or quadratic extrapolation in Ra is easy to implement. Assume that converged solutions $\mathcal{U}^{(0)}$, $\mathcal{U}^{(1)}$, $\mathcal{U}^{(2)}$ have been found for Rayleigh numbers $Ra^{(0)}$, $Ra^{(1)}$ and $Ra^{(2)}$. We can determine coefficients a_i , b_i , c_i such that

$$\mathcal{U}_i = a_i Ra^2 + b_i Ra + c_i \quad (17)$$

where i ranges over both the gridpoints and the components (H, U_r, U_θ, U_z). We then use (17) to compute an initial condition for Newton iteration at the new value $Ra^{(3)}$ given in (16). (The condition number of the 3×3 system (17) for a_i , b_i , c_i is improved if we subtract from Ra the average of the three Ra values.) Over many portions of many branches we find we can easily take $\Delta Ra \geq 200$. As an example, we computed the marigold branch which will be described in section IV E from $Ra = 2100$ to $Ra = 18000$, with intervals ΔRa varied dynamically between 10 and 1200 according to prescription (16), requiring a computation time of 1200 CPU seconds on the NEC SX-8.

Quadratic extrapolation, while not necessary for moving along a branch, proves essential near a turning point. Near a turning point $(Ra^{TP}, \mathcal{U}^{TP})$, we stop using extrapolation in Ra , as in (16), and instead use extrapolation in one of the components of \mathcal{U} . That is, we fix the value of one component, \mathcal{U}_I , and treat Ra as a dependent variable. To determine whether we are near a turning point, we use the fact that

$$|\mathcal{U}_i - \mathcal{U}_i^{TP}| \sim \sqrt{|Ra - Ra^{TP}|} \quad (18)$$

so that $\Delta \mathcal{U}_i$ must eventually exceed ΔRa as a turning point is approached. We monitor the relative changes by comparing the quantities

$$\left| \frac{\Delta \mathcal{U}_i}{\mathcal{U}_i} \right| \equiv \left| \frac{\mathcal{U}_i^{(1)} - \mathcal{U}_i^{(2)}}{\mathcal{U}_i^{(2)}} \right| \quad \text{with} \quad \left| \frac{\Delta Ra}{Ra} \right| \equiv \left| \frac{Ra^{(1)} - Ra^{(2)}}{Ra^{(2)}} \right|, \quad (19)$$

where γ is a multiplicative weighting factor ranging between 5 (to favor extrapolation in Ra) and 0.001 (to favor extrapolation in \mathcal{U}_i). When $|\Delta\mathcal{U}_i/\mathcal{U}_i|$ exceeds $\gamma|\Delta Ra/Ra|$, we replace (16), prescribing extrapolation in Ra , by extrapolation in \mathcal{U}_I :

$$\mathcal{U}_I^{(3)} = \mathcal{U}_I^{(2)} + \Delta\mathcal{U}_I = \mathcal{U}_I^{(2)} + \alpha(\mathcal{U}_I^{(2)} - \mathcal{U}_I^{(1)}). \quad (20)$$

We use the three previous converged fields and Rayleigh numbers to determine coefficients a_i, b_i, c_i for $i \neq I$ and a_{Ra}, b_{Ra}, c_{Ra} such that

$$\mathcal{U}_i = a_i \mathcal{U}_I^2 + b_i \mathcal{U}_I + c_i, \quad Ra = a_{Ra} \mathcal{U}_I^2 + b_{Ra} \mathcal{U}_I + c_{Ra} \quad (21)$$

and then use (21) to compute a new Ra and $\mathcal{U}_i, i \neq I$ corresponding to the \mathcal{U}_I prescribed by (20). This allows us to change direction in Ra ; (21) may lead to $Ra^{(3)} - Ra^{(2)}$ of opposite sign to that of $Ra^{(2)} - Ra^{(1)}$, unlike in equation (16).

The procedure above treats \mathcal{U}_I as an independent variable (as prescribed in equation (20)) and Ra as a dependent variable (as prescribed in equation (21)) in the predictor step (initialization). In this investigation, we have left the corrector step (Newton iteration) unchanged, that is, Ra remains unaltered by (10a). One strategy we have employed is to relax the tolerances near the turning point, for example to $\epsilon_{\text{Newton}} = 10^{-13}$ and $\epsilon_{\text{BCGS}} = 10^{-8}$. Like Xin [12], we have succeeded in traversing a number of turning points in this way, despite the near-singularity of the matrix $(\mathcal{B}_\mathcal{U} - I)$ near a bifurcation point.

D. Linear stability analysis

Once branches have been computed, we wish to determine their stability. In order to perform linear stability analysis of a steady state $\mathcal{U} \equiv (H, \mathbf{U})$, we carry out time integration of the Boussinesq equations linearized about \mathcal{U} for an infinitesimal perturbation $u \equiv (h, \mathbf{u})$:

$$\frac{du}{dt} = \mathcal{L}u + \mathcal{N}_\mathcal{U}u \quad (22)$$

We use the same timestepping formula (7) as for the nonlinear problem:

$$u(t + \Delta t) = (I - \Delta t \mathcal{L})^{-1} (I + \Delta t \mathcal{N}_\mathcal{U}) u(t) \equiv \mathcal{B}_\mathcal{U} u(t) \quad (23)$$

by carrying out the substitutions in (12). Since

$$\mathcal{B}_\mathcal{U} \approx \exp(\Delta t (\mathcal{L} + \mathcal{N}_\mathcal{U})) \quad \text{for } \Delta t \ll 1, \quad (24)$$

the eigenvalues λ of $\mathcal{B}_\mathcal{U}$ and eigenvalues σ of $\mathcal{L} + \mathcal{N}_\mathcal{U}$ are related via

$$\lambda \approx \exp(\sigma \Delta t) \iff \sigma \approx \frac{1}{\Delta t} \log |\lambda| \quad \text{for } \Delta t \ll 1 \quad (25)$$

The stability of \mathcal{U} is determined by the sign of the leading eigenvalue σ_{max} (that with largest real part) of $\mathcal{L} + \mathcal{N}_\mathcal{U}$, which corresponds to the dominant eigenvalue λ_{max} (that with largest magnitude) of $\mathcal{B}_\mathcal{U}$. Equation (23) prescribes acting with the linear operator $\mathcal{B}_\mathcal{U}$ on $u(t)$; when repeated over many Δt 's, u will converge to the eigenvector corresponding to λ_{max} , which is itself approximated by the Rayleigh quotient

$$\lambda_{\text{max}} \approx \lim_{t \rightarrow \infty} \frac{\langle u(t), \mathcal{B}_\mathcal{U} u(t) \rangle}{\langle u(t), u(t) \rangle}. \quad (26)$$

To determine several leading eigenvalues, the power method is generalized to the Arnoldi-Krylov method [11]. This consists of orthonormalizing a small number of fields

$$\{u(t=0), u(t=T), u(t=2T) \dots u(t=(K-1)T)\} \quad (27)$$

to create vectors $v_1, v_2, v_3, \dots v_K$, and then a small Hessenberg matrix $H_{jk} \equiv \langle v_j, \mathcal{B}_\mathcal{U} v_k \rangle$, which is directly diagonalised. Its eigenvalues approximate eigenvalues λ of $\mathcal{B}_\mathcal{U}$, while its eigenvectors ϕ consist of coefficients of the vectors v_j , to be combined to form approximate eigenvectors $\Phi \equiv \sum_j \phi_j v_j$ of $\mathcal{B}_\mathcal{U}$. The accuracy of these approximate eigenpairs is measured by the residue $\|\mathcal{B}_\mathcal{U} \Phi - \lambda \Phi\|$ in the case of complex eigenvalues. The integration of (23) is continued until the residues of the desired eigenvalues are below some acceptance criterion, usually near 10^{-6} .

The timestep required is similar to that for timestepping. One obvious restriction comes from the explicit scheme used in (23) for \mathcal{N}_U ; a timestep which violates this stability requirement leads to approximate eigenvalues of \mathcal{B}_U which bear no resemblance to those of $\exp(\Delta t(\mathcal{L} + \mathcal{N}_U))$. For smaller Δt , the accuracy of the eigenvalues depends on Δt because of the approximation (24). In particular, the time-splitting error means that \mathcal{B}_U is not a function of $\mathcal{L} + \mathcal{N}_U$. (In contrast, the errors in the pitchfork and turning point bifurcation thresholds obtained by Newton's method result only from the spatial discretization.) We have used $\Delta t = 10^{-3}$ for $Ra \lesssim 10\,000$ and $\Delta t = 5 \times 10^{-4}$ for $Ra > \text{sim}10\,000$. We estimate our accuracy in locating bifurcation points and stability ranges to be $\Delta Ra \lesssim 1$. We used $K = 10$ vectors and a time interval of $T = 100\Delta t$, i.e. $T = 0.1$ or $T = 0.05$ to create the Krylov vectors (27), and an acceptance criterion for the residues of 10^{-6} .

A method which produces approximate eigenvalues which are independent of Δt is the inverse Arnoldi method [9], in which (23) is replaced by

$$u^{n+1} = (\mathcal{L} + \mathcal{N}_U)^{-1} u^n. \quad (28)$$

This is accomplished in practice by solving the equation

$$(\mathcal{B}_U - I)u^{n+1} = \Delta t(I - \Delta t\mathcal{L})^{-1} u^n \quad (29)$$

The equivalence between (28) and (29) follows from a calculation similar to (9). Equation (29) is very similar to (10a) and is also solved by BiCGSTAB. Only a few iterations (between 1 and 10) of (29) lead to an extremely accurate eigenvalue. However, the inverse Arnoldi is more difficult to implement than the exponential Arnoldi method. For this reason, we have chosen not to do so for this study.

IV. RESULTS

A. Bifurcation Diagram

Using the methods described in section III, we have succeeded in continuing the branches we found previously via time integration [3, 4]. By going around turning points and bifurcation points, we have computed a total of 17 branches of convective steady states. These are related to the conductive state and to each other by 5 primary and 3 secondary pitchfork bifurcations, and 8 saddle-node bifurcations. The bifurcation diagram is shown in figure 2. Tables summarizing all of the branches and bifurcations we have found are given in section V.

The axes of figure 2 have been chosen with care. In order to show the full extent of our calculations in Rayleigh number and, at the same time, distinguish between various low-Rayleigh-number primary bifurcations, figure 2 uses a logarithmic scale in Ra . More specifically, using $\log(Ra - 1000)$ distinguishes primary bifurcations better than $\log Ra$. The vertical axis was chosen to best distinguish between the various branches. The quantity \bar{H} is the maximum absolute value of the temperature deviation over the ring at $(r = 0.3, \theta, z = 0)$

$$\bar{H} \equiv \max_{\theta} |H(r = 0.3, \theta, z = 0)|. \quad (30)$$

\bar{H} itself and the commonly used Nusselt number deviation

$$Nu - 1 = \int r dr d\theta \partial_z H(r, \theta, z = 0) - 1 \quad (31)$$

have a strong linear dependence on Ra ; plotting them directly as a function of Ra does little to separate the branches. We have therefore chosen instead to represent each state by its value of \bar{H}/Ra . (Exceptionally, for the first two-tori branch, we have plotted $-\bar{H}/Ra$ for low Ra to avoid a reversal in slope due to the absolute value in (30).) Each branch in figure 2 is a representative of a number of branches – the group orbit – that can be obtained by reflection and rotations.

In order to understand the complicated bifurcation diagram in figure 2, we will select various aspects for detailed study below.

B. Primary Bifurcations

We give in table I the first critical wavenumber and Rayleigh number pairs. The thresholds given to $\Delta Ra = 0.1$ are extrapolations from the branches calculated using Newton's method. The thresholds given as integer values were

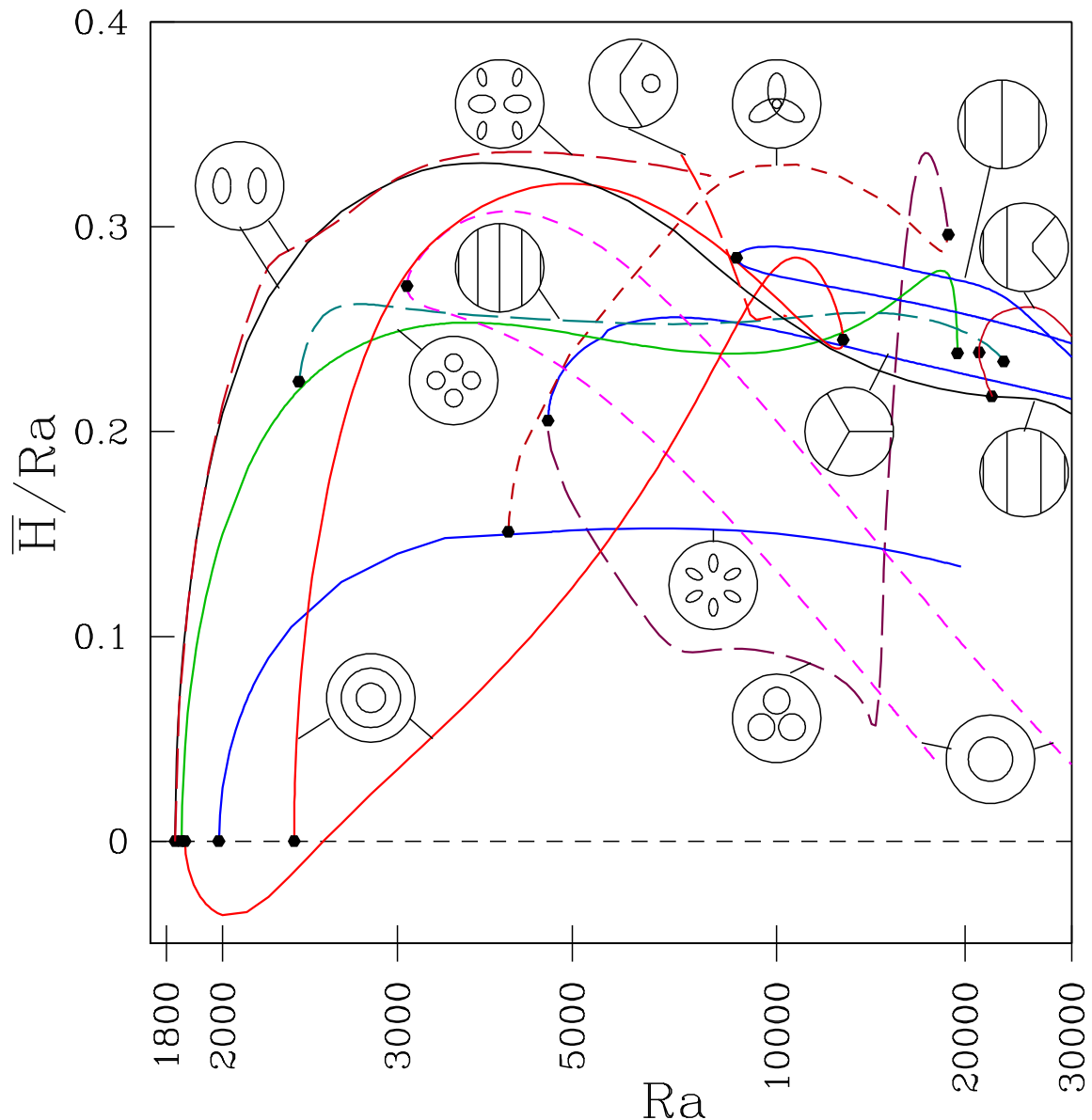


FIG. 2: (Color online) Bifurcation diagram containing 17 branches of steady states, in addition to the conductive branch (indicated by short-dashed horizontal line). Shown are pizza (solid green), four-roll (long-dashed turquoise), two-tori (solid red; 2), torus (long-dashed magenta; 2), marigold (solid blue), mitsubishi (short-dashed purple), cloverleaf (long-dashed purple) and mercedes (solid black), three-roll (solid black), tiger (long-dashed brick), asymmetric three-roll (solid brick; 2), two-roll (solid blue; 2), CO (long-dashed red) branches. The notation “torus (long-dashed magenta; 2)”, e.g., signifies that there are 2 torus branches, related by saddle-node bifurcations and both shown as long-dashed magenta curves. Note that the bifurcation diagram gives no information concerning stability; i.e. whether a solution curve is depicted as solid or dashed does not indicate its stability. Turning points or pitchfork bifurcations are shown as dots.

calculated from the linear stability analysis of the conductive branch. In the remainder of the manuscript, we round Rayleigh numbers to integer values (except in a few very specific cases). Our thresholds agree quite well with those of previous researchers. The discrepancies are typically on the order of 0.3% with the calculations of Ma *et al.* [7] and on the order of 0.02% with those of Martin-Witkowski [13], which we believe to be the two most recent threshold calculations in this geometry. With increasing Rayleigh number, many other bifurcations occur from the conductive state, both to higher wavenumbers and to different eigenmodes with the same wavenumbers. The branches created at such bifurcations are necessarily unstable.

It is the first four bifurcations of table I, along with the last column, which will prove relevant to the steady states observed, i.e. the stable ones. In figure 3 we show these first bifurcations, along with corresponding nonlinear states

Ra	1828.4	1849.4	1861.6	1985.3	2055	2172	2255	2328.0
m	1	2	0	3	4	5	1	0

TABLE I: (Color online) First bifurcations from conductive state

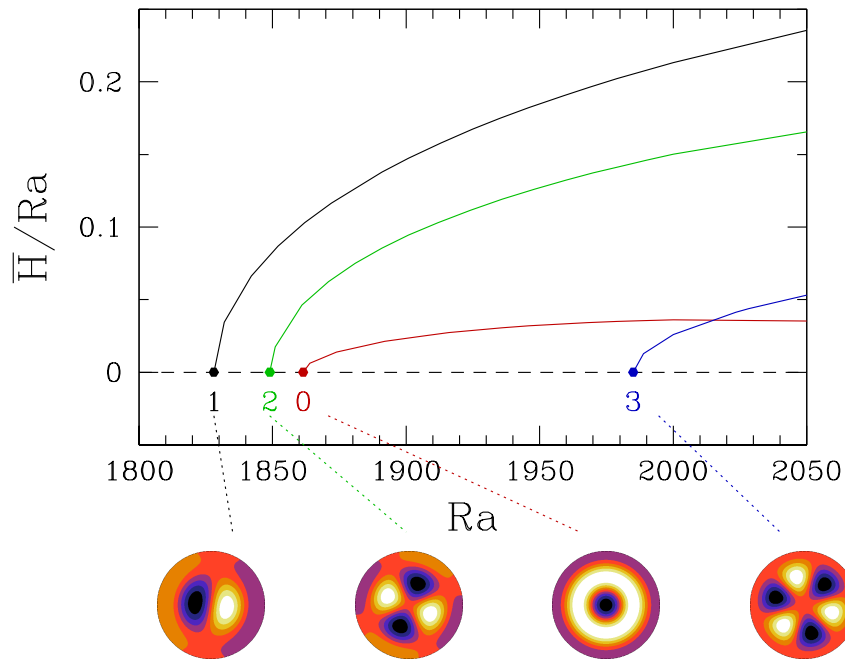


FIG. 3: (Color online) Primary branches bifurcating from conductive state. For this aspect ratio, $\Gamma = 2$, and with insulating lateral walls, the first four critical wavenumber and Rayleigh number pairs are $(m = 1, Ra = 1828; \text{black})$, $(m = 2, Ra = 1849; \text{green})$, $(m = 0, Ra = 1861; \text{red})$, and $(m = 3, Ra = 1985; \text{blue})$. Below are representative states from each of the bifurcating branches.

at slightly supercritical values of Ra . We recognize the dipole, pizza and two-tori states. The other states in figures 1 and 2 – the two-, three-, and four-roll states, or the torus, mercedes, and CO states – are not present in figure 3. Their origin is addressed in the sections which follow.

C. Pizza and Four-roll branches ($m = 2$)

We now focus on various sets of solution branches. We begin with the branches arising from the instability to an $m = 2$ quadrupolar eigenvector at $Ra = 1849$, because these are free from the complications which we will encounter for the other azimuthal wavenumbers. We use three figures to describe the structure of these branches. Figure 4 uses the same coordinates as figure 2, merely extracting the relevant branches. Figure 5 is a qualitative bifurcation diagram, accompanied by illustrations of representative states along the branches. Finally, figure 6 shows leading eigenvalues, from which the stability of the underlying branches can be deduced.

The bifurcation sequence is best understood by studying figure 5. The schematic quantity along the vertical axis and the monotonic but non-uniform Rayleigh-number progression along the horizontal axis, are chosen to separate the different branches and to illustrate the bifurcations. Representative states along the branches are illustrated via temperature distributions in the midplane ($z = 0$), with light portions representing hot rising fluid and dark portions representing cold descending fluid. To avoid further cluttering the figure, the Rayleigh numbers given for the representative states have been rounded to the nearest 10, 100 or even 1000, with precise bifurcation points given along the axis. The azimuthal orientation of the representative states is arbitrary, and to each branch corresponds another branch obtained by the Boussinesq reflection symmetry which, for these illustrations, would mean reversing light and dark.

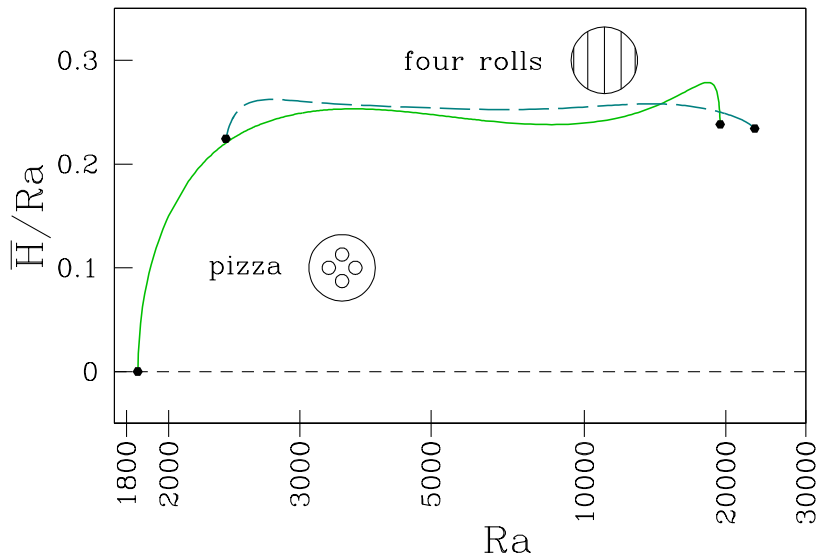


FIG. 4: (Color online) Partial bifurcation diagram including $m = 2$ primary branch and connecting branches. Bifurcations are shown as dots. The primary **Pizza** branch (solid, green) bifurcates from the conductive state at $Ra = 1849$ and terminates in a saddle-node bifurcation at $Ra \approx 19450$. The **Four-roll** branch (dashed, turquoise) bifurcates from the pizza branch at $Ra = 2353$ and terminates at a saddle-node bifurcation at $Ra \approx 23130$.

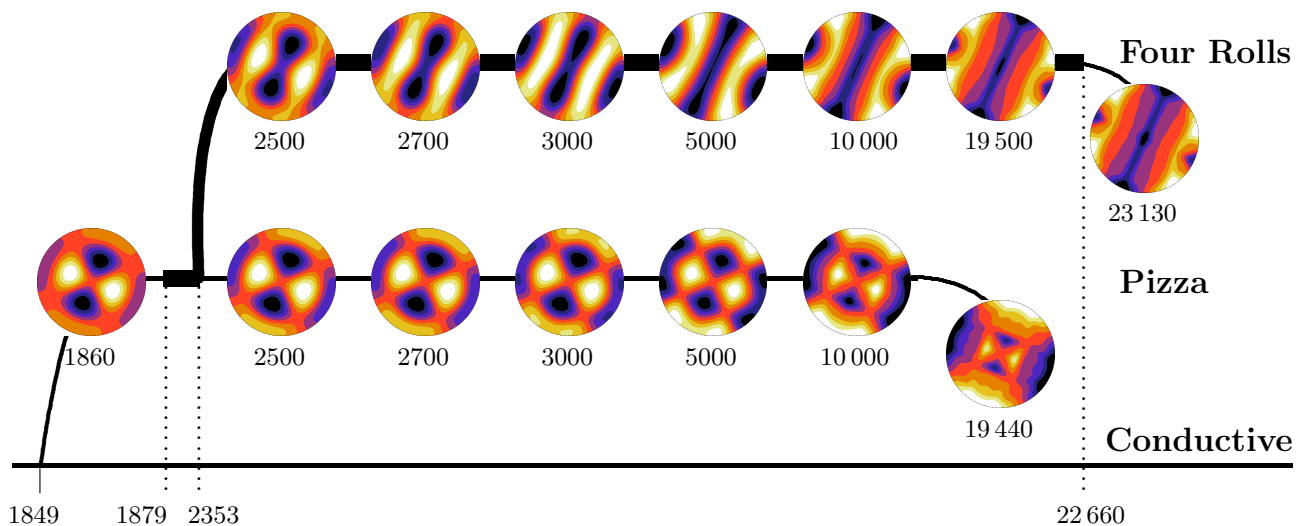


FIG. 5: (Color online) Schematic partial bifurcation diagram relating branches originating from the $m = 2$ bifurcation. At $Ra = 1849$ the **Pizza** branch originates via a circle pitchfork bifurcation from the conductive state corresponding to an $m = 2$ eigenvector. It terminates at a turning point at $Ra \lesssim 19450$ and is stable for $1879 \leq Ra \leq 2353$. At $Ra = 2353$, a secondary pitchfork bifurcation leads to a **Four-roll** branch, which is stable for $Ra \lesssim 22660$ and ends at a turning point at $Ra \approx 23130$. For visual clarity, the Rayleigh numbers given for the representative states have been rounded to the nearest 10, 100 or 1000.

A circle pitchfork bifurcation from the **Conductive** branch to an $m = 2$ eigenmode takes place at $Ra = 1849$. Figure 5 shows that, near onset, the states along the branch created by this bifurcation contain two hot upwelling spots and two cold downwelling spots. Their resemblance to a small pizza leads us to call this the **Pizza** branch. As Ra increases, the central convective regions shrink. By the time the pizza branch terminates at a saddle-node bifurcation at $Ra = 19450$, most of the convection takes place at four regions along the edge of the container.

A pitchfork bifurcation at $Ra = 2353$ from the pizza branch breaks the symmetry between hot upwelling and cold downwelling fluid: the two downwelling spots merge as the two upwelling spots elongate (or vice versa for the complementary branch, not shown). This secondary bifurcation is also computed by Ma [7], who gave its threshold as $Ra = 2350$. The pitchfork bifurcation leads to a **Four-roll** branch which terminates at a saddle-node bifurcation at $Ra \approx 23130$. Along the four-roll branch, the convective regions diminish as Ra increases, as was the case for the

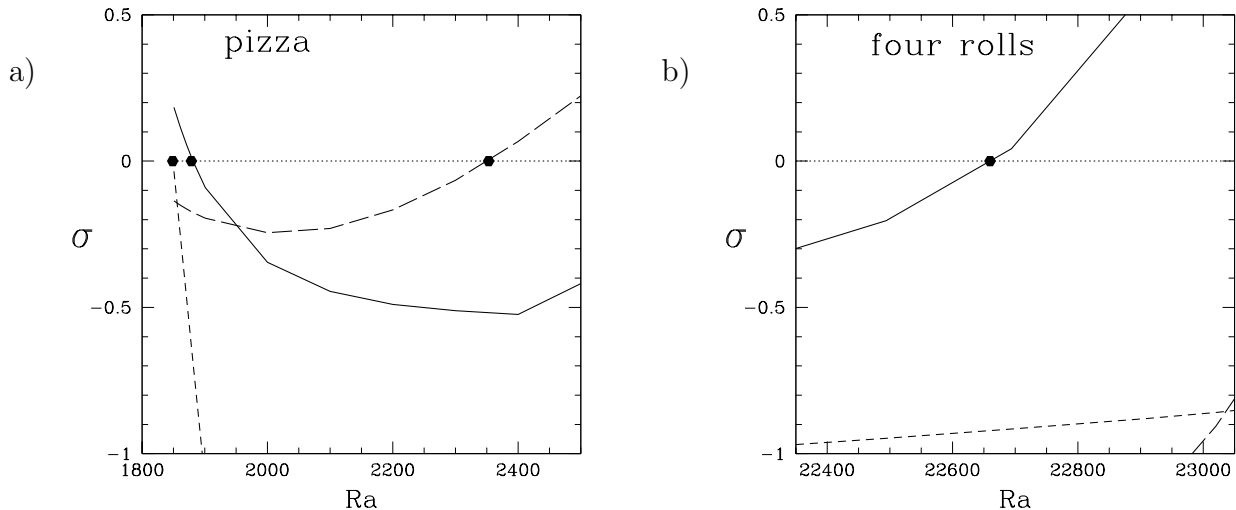


FIG. 6: Four leading eigenvalues of (a) the pizza branch at low Ra and of (b) the four-roll branch at high Ra . Bifurcations (zero crossings) indicated by dots. The zero eigenvalue (dotted) which exists throughout corresponds to the marginal stability to rotation of the pattern. a) The bifurcating eigenvalue (short-dashed) decreases steeply from 0 at onset, $Ra = 1849$. The pizza branch is initially unstable since it inherits the unstable eigenvalue (solid) of the conducting branch, due to the preceding $m = 1$ bifurcation. This leading eigenvalue decreases with Ra , crossing zero at $Ra = 1879$. Another eigenvalue (long-dashed) becomes positive at $Ra = 2353$, accompanying the bifurcation to the four-roll branch. The stability interval of the pizza branch is $1879 \leq Ra \leq 2353$. b) The four-roll branch loses stability near $Ra = 22660$.

pizza branch; the rolls become wide, with narrow upwelling and downwelling boundaries.

Figure 6a shows the four leading eigenvalues of the pizza branch near onset, computed by the methods described in section III D. They are grouped into distinct sets by examining the spatial structure, especially the azimuthal wavenumber spectrum, of the corresponding eigenvectors, and then plotted as curves. Very near onset, each eigenvalue can be associated with an azimuthal wavenumber, since it is connected to an eigenvalue of the conductive branch. The zero eigenvalue ($m = 2$, sometimes called the phase mode) which exists throughout corresponds to the marginal stability to rotation of the pattern. The eigenvalue which is zero at onset and then rapidly decreases is that corresponding to the circle pitchfork which creates this branch (also $m = 2$, sometimes called the amplitude mode). The positive eigenvalue ($m = 1$) at onset results from the fact that the bifurcation to the dipole branch at $Ra = 1828$ precedes the creation of the pizza branch. The pizza branch inherits this instability when it is created at $Ra = 1849$ and becomes stable at $Ra = 1879$, when the leading eigenvalue becomes negative, as shown in figure 6a. This confirms our time-dependent simulations [3, 4], summarized in figure 1, which shows the pizza branch as stable at $Ra = 2000$. However, it enjoys only a short Ra -interval of stability, as another eigenvalue (connected to the $m = 0$ eigenvalue of the conductive branch) becomes positive at $Ra = 2353$, when the secondary pitchfork bifurcation creates the four-roll branch.

Figure 6b shows that the four-roll branch remains stable until $Ra \lesssim 22660$, a far wider Rayleigh-number interval than the pizza branch. Indeed, roll states are preferred by convective systems and are those generally observed in experiments and time-dependent simulations. In particular, a four-roll state was computed in time-dependent simulations [3, 4] for Ra between 5000 and 20000 (see figure 1) and is one of the five states observed experimentally by Hof *et al.* [1] at $Ra = 14200$.

As explained in section II B, the four-roll states have symmetry group D_2 : they are invariant under rotation by π and reflection in either of the symmetry axes, as stated in (5a)–(5b). The pizza states are also invariant under the additional symmetry given in (5c) (rotation by $\pi/2$, $z \rightarrow -z$, $U_z \rightarrow -U_z$, $H \rightarrow -H$) so have the larger symmetry group $D_2 \times Z_2$, as is typical for the primary branches bifurcating from the conductive state.

D. Torus and two-tori branches ($m = 0$)

We now survey the axisymmetric branches. Figure 7 extracts the axisymmetric branches from the complete bifurcation diagram of figure 2. There are two pairs of branches, i.e. a total of four branches of axisymmetric states. A

schematic bifurcation diagram showing representative states is given in figure 8 and leading eigenvalues are shown in figure 9.

The **Two-tori** branches result from two pitchfork bifurcations from the conductive state at $Ra = 1862$ and $Ra = 2328$. These two branches meet and annihilate at a turning point at $Ra = 12711$. Most of the states along these branches contain two concentric toroidal convection rolls. The branch created at $Ra = 1862$, which we call the upper or stable two-tori branch, is the more stable of the two. In fact, it is unstable when it is first created, as shown in figure 9, since the $m = 1$ and $m = 2$ bifurcations precede the $m = 0$ bifurcation. For an axisymmetric convective state, the eigenvectors are each associated with a single azimuthal wavenumber m . The bifurcating eigenvalue, with $m = 0$, is 0 at onset and rapidly decreases. One of the two leading eigenvalues becomes negative at $Ra = 2116$ ($m = 2$) and the second at $Ra = 2300$ ($m = 1$), stabilizing this two-tori branch. These stabilizing bifurcations were also computed by Ma *et al.* [7], with thresholds 2113 and 2245, respectively. The upper two-tori branch remains stable until $Ra = 5438$, when the $m = 1$ eigenvalue becomes positive again.

The **One-torus** branches emerge from a saddle-node bifurcation at $Ra = 3076$. The states on these branches all contain a single toroidal convection roll. We have not found any connection between these branches and any others, including the conductive branch. Both branches are initially unstable. The lower one-torus branch never stabilizes and we have been unable to calculate it past $Ra = 17857$. The upper or stable one-torus branch is created with five positive eigenvalues. As Ra increases, these successively become negative, as shown in figure 9. The branch is stable for $Ra \geq 4918$ and exists until at least $Ra = 29940$. It is clear that the axisymmetric state observed at $Ra = 14200$ in experiment [1] and in time-dependent simulation [3, 4, 6, 7] must be on the stable one-torus branch, and not on the two-tori branch (which is unstable for $Ra > 5438$ and does not exist for $Ra > 12711$) which bifurcates from the conductive state.

Along the upper two-tori branch the inner roll dominates, while along the lower two-tori branch, the outer roll dominates. These states do not necessarily all contain two rolls. In particular, some states along the lower two-tori branch for $Ra \lesssim 5000$ seem to contain only one roll. These states bear a qualitative and quantitative resemblance to those on the upper one-torus branch. On figure 7, the upper one-torus and the lower two-tori branches are nearly tangent to one another over the interval $3000 \lesssim Ra \lesssim 3500$, while at the turning point at $Ra = 3076$, the one-torus states bear a strong resemblance to the lower two-tori branch.

The axisymmetric convective branches break the Boussinesq symmetry (4c), while retaining the $O(2)$ azimuthal symmetry (4a)-(4b).

E. Mercedes, Cloverleaf, Mitsubishi and Marigold states ($m = 3$)

The set of branches with three-fold symmetry are perhaps the most interesting, and certainly the most aesthetic. We have been able to trace the tortuous connection between the states obtained by time-integration (and hence necessarily stable) and the $m = 3$ primary branch (which, occurring after three other primary bifurcations, is necessarily unstable). Figure 10 extracts from figure 2 the branches with three-fold symmetry. Four branches are present (in addition to the conductive branch), connected by saddle-node and pitchfork bifurcations, shown as dots. Figure 11 plots the leading eigenvalues of these four branches. The qualitative bifurcation diagram in figure 12 provides a clearer picture of the bifurcations, without the crossings present in figure 10. We recall that an identical set of branches, with hot and cold reversed (along with upwelling and downwelling) also exists, and that the azimuthal orientation is arbitrary.

We begin by describing the states in figure 12, beginning from the stable state at $Ra \approx 30000$, which Hof called **Mercedes** because of its resemblance to the logo of this automobile [2]. This state was observed in Hof's experiment [1] and in time-dependent simulations [3, 4], where it was computed for Ra between 5000 and 29000, as shown in figure 1. A mercedes state was also computed at $Ra = 31250$ by Leong [6] and at $Ra = 14200$ by Ma *et al.* [7]. For high Ra , the hot upwelling and cold downwelling regions in the midplane are narrow, confined to three hot spots along the lateral boundary and a central cold Y-shaped region. With decreasing Ra , the upwelling and downwelling regions come to occupy an increasing portion of the midplane. By the turning point at $Ra = 4634$, the three hot spots have widened, becoming almost circular, and the center and extremities of the cold Y have widened into four triangles. Emerging from this turning point is what we have called the **Cloverleaf** branch. Following this branch towards increasing values of Ra , the three hot spots move inwards from the boundary and the cold Y-shaped region breaks, leaving four separate triangles. The hot spots and the central cold triangle become smaller, while the three remaining cold triangles narrow and cling to the lateral boundary. By the turning point at $Ra = 18762$, the hot spots have merged into one central triangular region, and the cold regions form a ring occupying almost the entire circumference. As we follow the new branch with decreasing Ra , the points of the triangle expand and separate, forming oval petals or blades, while the exterior ring forms three exterior triangles. Midway along this branch, the states resemble the logo of the **Mitsubishi** automobile, and this is the name we have given to the branch. The hot uprising and cold downwelling regions become more similar as Ra decreases. At $Ra = 4103$, the Mitsubishi branch is seen to emanate

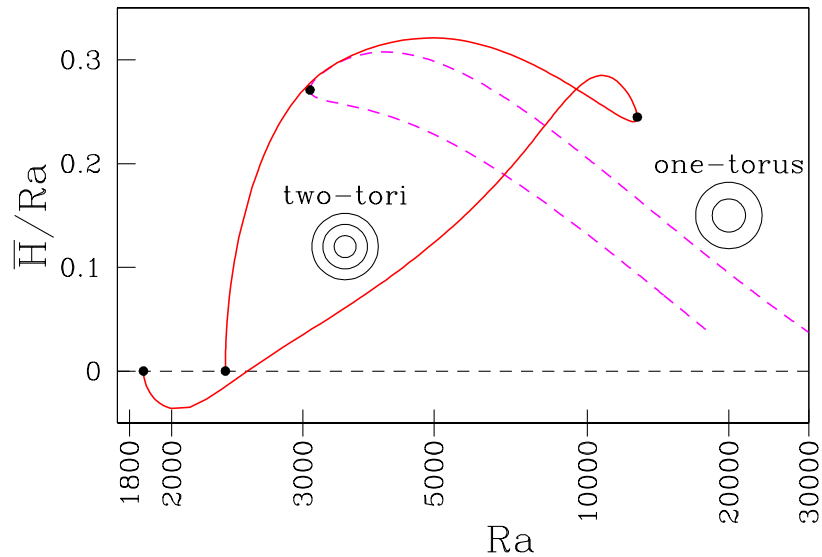


FIG. 7: (Color online) Partial bifurcation diagram including only axisymmetric states. The **Two-tori** branches (dashed, magenta) emerge from pitchfork bifurcations from the conductive branch at $Ra = 1861.5$ and $Ra = 2328$. They join and terminate at a turning point at $Ra = 12711$. The **One-torus** branches (solid, red) emerge from a turning point at $Ra = 3076$ and seem to be unconnected to the conductive state.

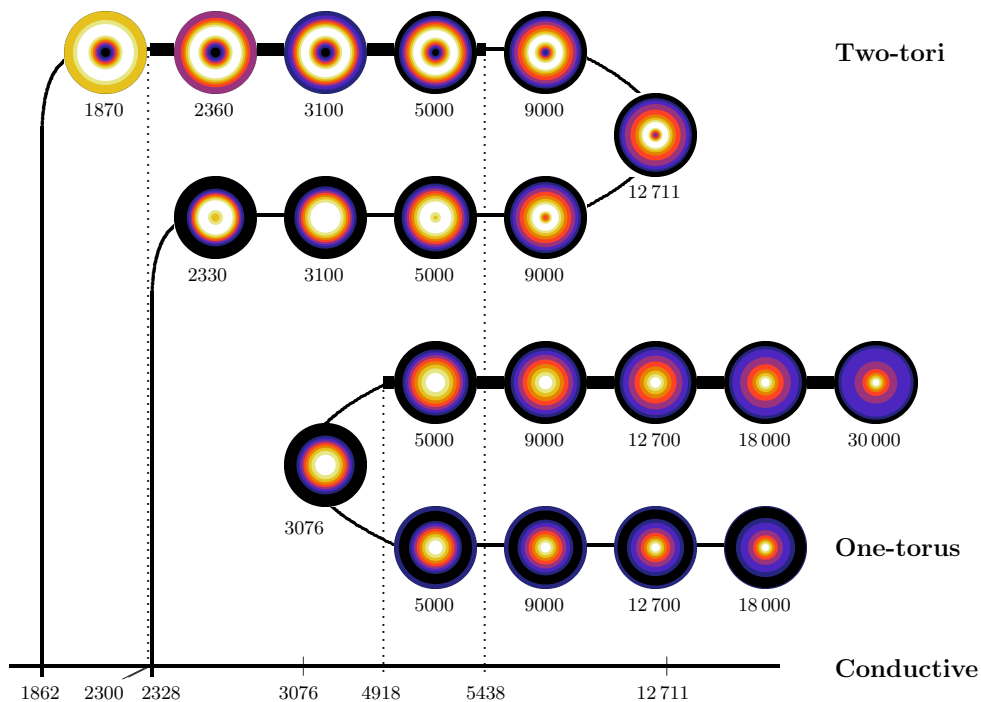


FIG. 8: (Color online) Schematic partial bifurcation diagram showing axisymmetric branches. The **Two-tori** branches are connected to the conductive branch via pitchfork bifurcations at $Ra = 1862$ and 2328 , and to each other via a turning point at $Ra = 12711$. The upper two-tori branch is stable for $2300 \leq Ra \leq 5438$. The **One-torus** branches are connected to each other via a turning point at $Ra = 3076$. The upper one-torus branch is stable for $Ra \geq 4918$. Most states along the two-tori branches contain two concentric rolls, but states on the lower two-tori branch resemble those on the upper one-torus branch for $Re \leq 3500$.

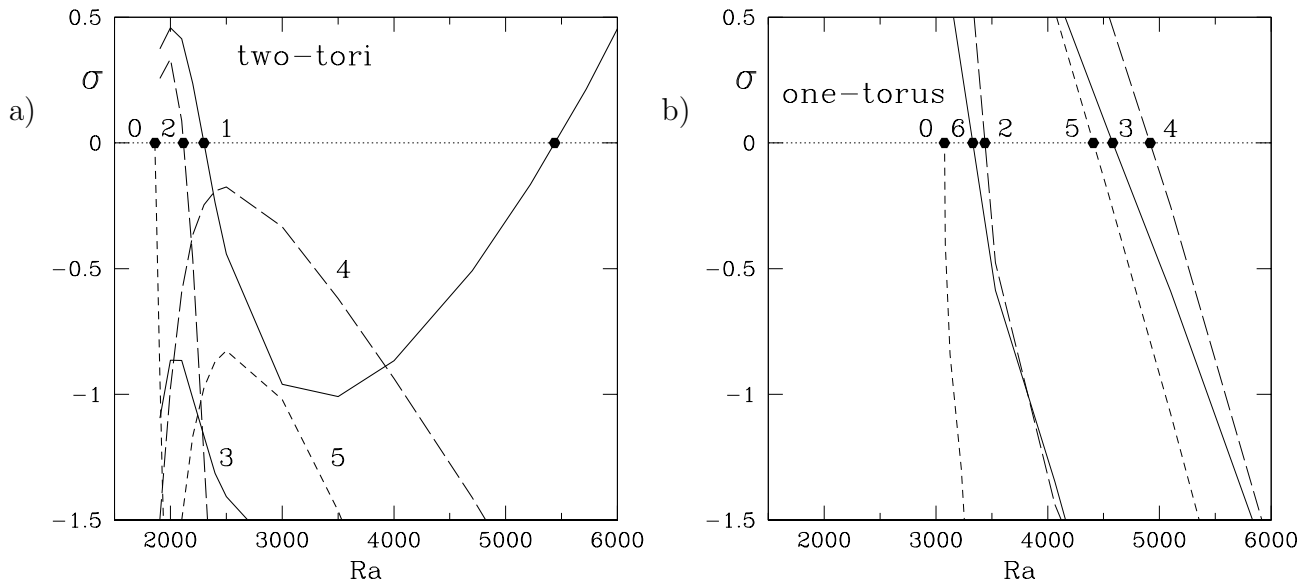


FIG. 9: Five leading eigenvalues of upper axisymmetric branches, each labelled with its azimuthal wavenumber m . a) The upper two-tori branch has two positive eigenvalues at onset at $Ra = 1862$, which cross zero at $Ra = 2116$ and $Ra = 2300$ and again at $Ra = 5438$. It is stable for $2300 \leq Ra \leq 5438$. b) The upper one-torus branch has five positive eigenvalues at onset at $Ra = 3076$. These cross zero at $Ra = 3330, 3438, 4408, 4582$ and 4918 , above which the branch is stable.

in a pitchfork bifurcation from the **Marigold** branch, whose states have six equal petal-shaped regions. The marigold branch itself is generated at a circle pitchfork bifurcation from the conductive branch at $Ra = 1985$.

The Mitsubishi, cloverleaf and Mercedes states have D_3 symmetry, while the marigold states have the larger symmetry group $D_3 \times Z_2$.

The cloverleaf and Mitsubishi branches were obtained from the Mercedes branch by going around the turning points via the quadratic extrapolation described in section III. Additional effort is required to switch from the Mitsubishi to the marigold branch, since straightforward continuation treats the pitchfork as it would a turning point. Because we can calculate eigenvectors, steady states and transient behavior, there are a number of ways in which a starting point on the marigold branch could be obtained:

(i) Take a Mitsubishi state, for which the left and right-hand-sides of (5c) are not equal, and average the two expressions.

(ii) Add a small amount of the $m = 3$ eigenvector to the conductive branch.

(iii) Carry out time-integration for $Ra > 1985$, retaining only azimuthal modes which are multiples of three.

We used method (iii), halting the integration after the marigold state was reached but before its instability was manifested.

Although figure 11 shows leading eigenvalues corresponding to the states of figure 10, it is of a different nature from the previous eigenvalue plots. Figures 6 and 9 showed one or more leading eigenvalues for states along a single branch. In contrast, figure 11 shows a single eigenvalue per state, but for states along the four different branches described above. Thus, between one and four eigenvalues are shown for a single Rayleigh number. All of the branches have at least one positive eigenvalue (and are thus unstable) except the Mercedes branch for $Ra > 5503$. When the marigold branch bifurcates from the conductive branch at $Ra = 1985$, it inherits three positive eigenvalues, the largest of which is the highest curve in figure 11. The Mitsubishi branch shares the spectrum of the marigold branch at the pitchfork bifurcation at $Ra = 4103$. As Ra increases, both branches become more unstable, but, for $Ra \gtrsim 12500$, the eigenvalues of the Mitsubishi branch eventually begin to decrease. The Mitsubishi branch is still unstable when it meets the cloverleaf branch at the turning point at $Ra = 18762$. Following the cloverleaf branch with decreasing Ra , the leading eigenvalue decreases. When the cloverleaf and Mercedes branches meet at the turning point at $Ra = 4634$, the leading eigenvalue is still barely positive. Following the Mercedes branch with increasing Ra , the leading eigenvalue continues to decrease, becoming negative and stabilizing the branch for $Ra > 5503$.

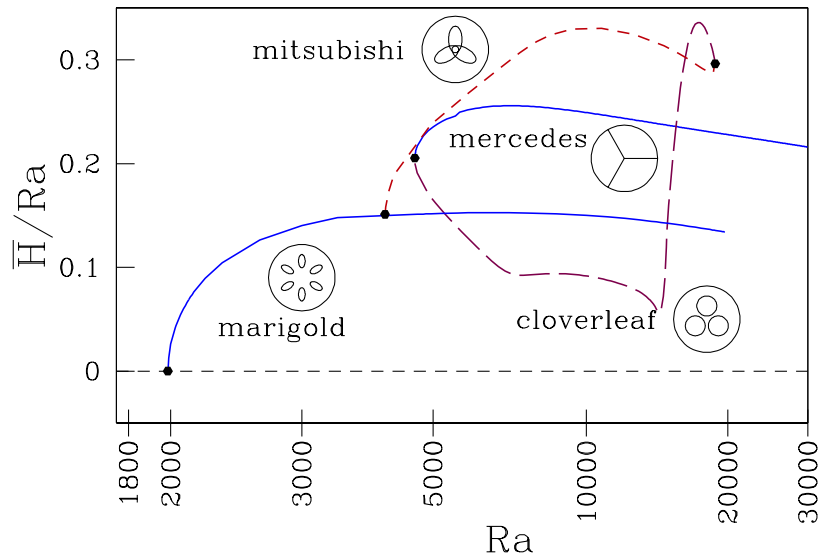


FIG. 10: (Color online) Partial bifurcation diagram including only branches with three-fold symmetry. The **Marigold** branch (solid, blue) arises at a pitchfork bifurcation from the **Conductive** branch (short-dashed, black) at $Ra = 1985$. A secondary pitchfork bifurcation from the marigold branch at $Ra = 4103$ gives rise to the **Mitsubishi** branch (short-dashed, lighter purple). At a turning point at $Ra = 18762$, it meets the **Cloverleaf** branch (long-dashed, darker purple). The **Mercedes** branch (solid, blue) originates at another turning point at $Ra = 4634$.

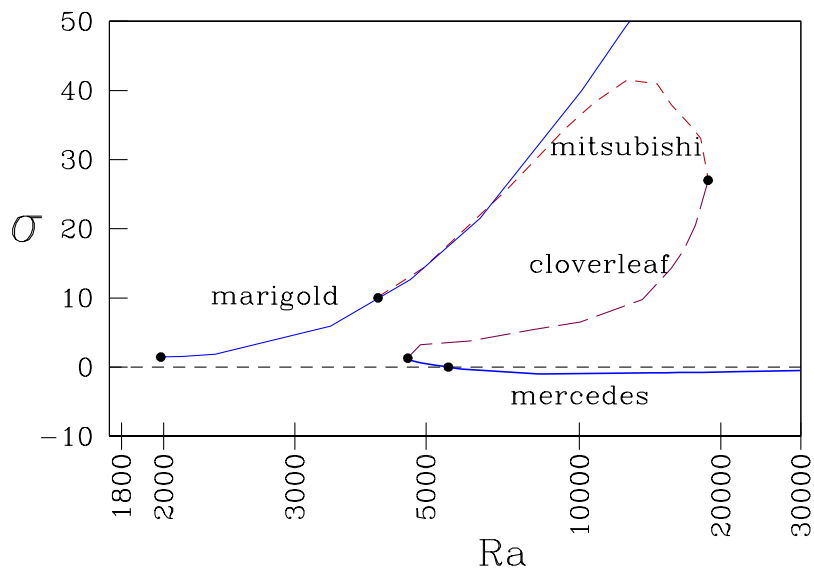


FIG. 11: (Color online) Leading eigenvalue for each of the three-fold-symmetric branches. From highest to lowest: marigold (solid, blue), Mitsubishi (short-dashed, light purple), cloverleaf (long-dashed, dark purple), Mercedes (solid, blue). Dots indicate bifurcations from conductive to marigold branch ($Ra = 1985$, $\sigma \approx 1.46$), to Mitsubishi branch ($Ra = 4103$, $\sigma \approx 10$), to cloverleaf branch, ($Ra = 18762$, $\sigma \approx 27$), to Mercedes branch ($Ra = 4634$, $\sigma \approx 1.3$), and final stabilization of Mercedes branch ($Ra = 5503$, $\sigma = 0$).

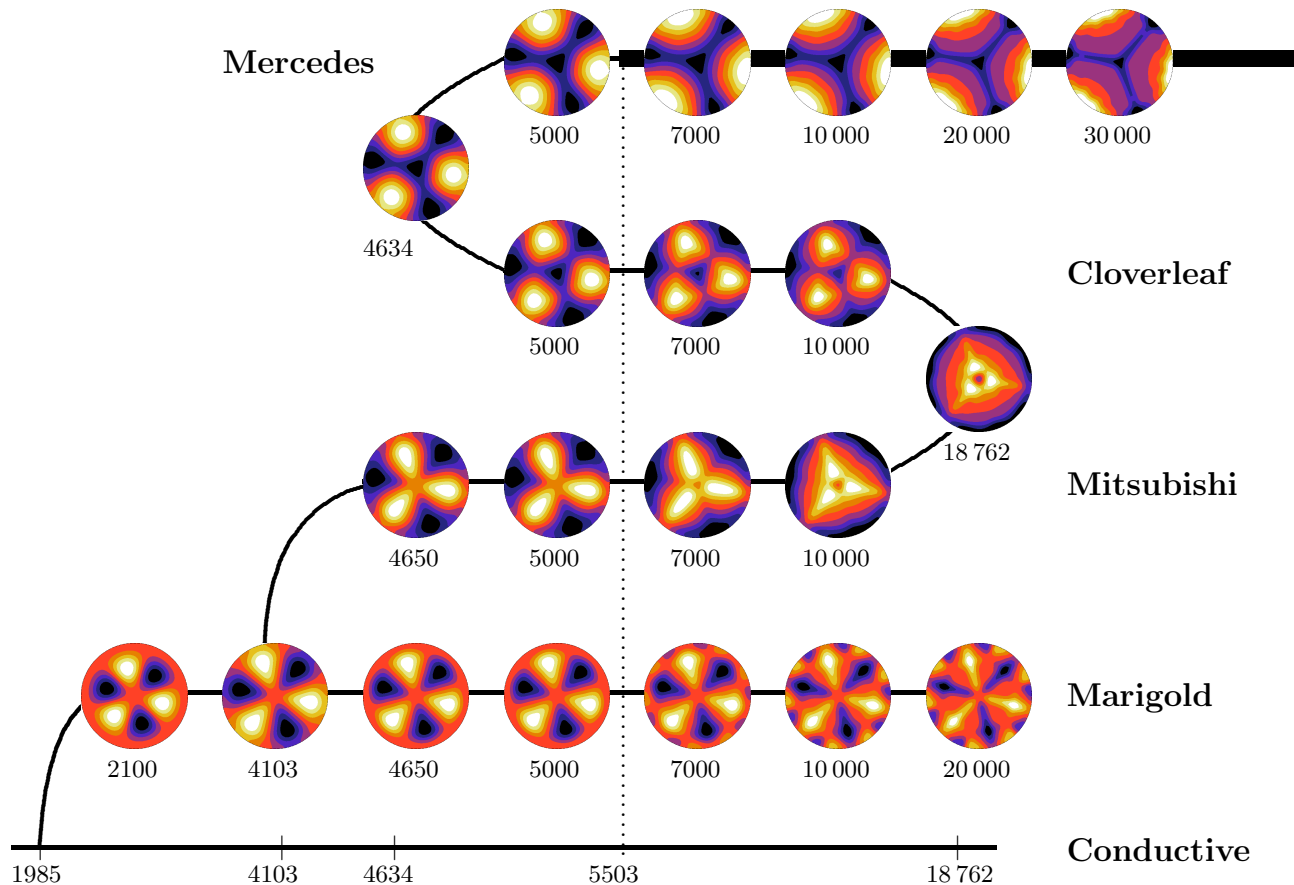


FIG. 12: (Color online) Schematic partial bifurcation diagram relating branches originating from the $m = 3$ bifurcation. The four branches of steady states with three-fold symmetry are the **Mercedes**, **Cloverleaf**, **Mitsubishi**, and **Marigold** branches. The Marigold branch is created by an $m = 3$ circle pitchfork bifurcation from the **Conductive** branch at $Ra = 1985$. It undergoes a pitchfork bifurcation at $Ra = 4103$, leading to the **Mitsubishi** branch. A turning point at $Ra = 18762$ leads to the **cloverleaf** branch, and another turning point at $Ra = 4634$ to the **Mercedes** branch. Only the Mercedes branch is stable, for $Ra > 5503$, as indicated by the thick line.

F. Dipole, Tiger and Three-roll branches ($m = 1$)

Although the $m = 1$ bifurcation has the lowest Rayleigh number threshold, $Ra = 1828$, we have postponed its discussion because of its odd behavior. Two branches bifurcate simultaneously, as shown in figures 13 and 14. The states close to the bifurcation are of dipole form, as expected. A dipole state is observed at $Ra = 2500$ by Leong [6] and by Ma *et al.* [7]. Along one branch, additional spots appear on either side of the dipole, which grow as Ra is increased; we have given the name of **Tiger** to this branch. We have been unable to compute the tiger branch above $Ra = 7936$. The other branch is more conventional. The two parts of the dipole elongate along the dipole axis and patches of opposite sign appear and elongate near the boundary, leading eventually to a **Three-roll** structure. The three-roll branch exists at least until $Ra = 30000$, where we have stopped our computations.

Time-dependent simulations [3, 4] between $Ra = 20000$ and 25000 show a transition to an **Asymmetric Three-roll** state, for which the rolls are slightly shifted. We have determined that an asymmetric branch emerges from the three-roll branch at $Ra = 22125$ via a subcritical pitchfork bifurcation (the only subcritical bifurcation we have found in this system). The branch reverses direction and stabilizes at a saddle-node bifurcation at $Ra = 21078$. Three-roll and asymmetric three-roll states are observed at $Ra = 12500$ and $Ra = 25000$, respectively, by Leong [6].

The tiger and the three-roll branches share the same spatial symmetry, that is $D_1 \times Z_2$, where D_1 (equivalent to Z_2) is generated by reflection in the axis perpendicular to the roll or dipole axis, as in (5b), and Z_2 is generated by simultaneous rotation by π and reflections $z \rightarrow -z$, $U_z \rightarrow -U_z$, $H \rightarrow -H$, as in (5c). The asymmetric three-roll branch has symmetry D_1 .

Figure 15a, containing leading eigenvalues of each branch near threshold, shows that the tiger branch becomes quite

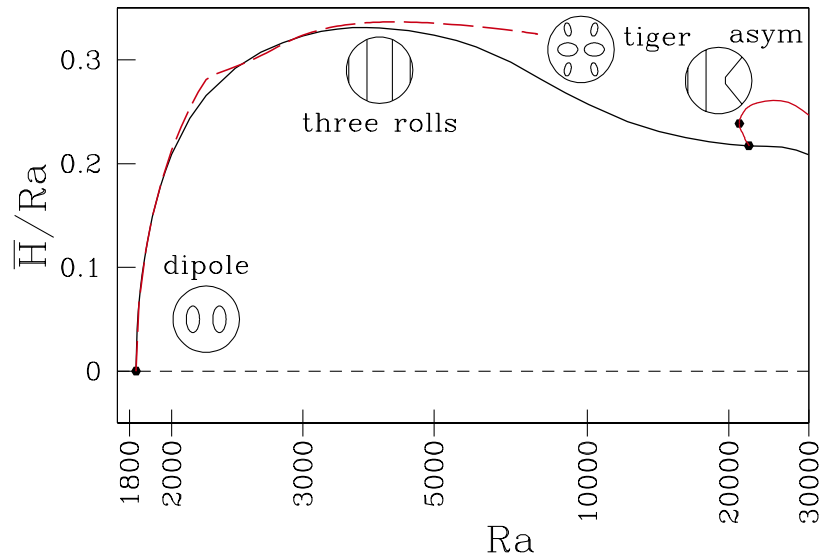


FIG. 13: (Color online) Partial bifurcation diagram of branches created at the $m = 1$ primary bifurcation. Two branches of dipole states are created at $Ra = 1828$, and seem to be tangent to one another near the bifurcation. As Ra increases, the spatial forms along these branches evolve in divergent ways. One branch contains the three-roll states (solid, black) and the other (dashed, brick) contains the tiger states. An asymmetric three-roll branch (solid, brick) is created at a subcritical pitchfork bifurcation at $Ra = 22155$ and reverses direction at a saddle-node bifurcation at $Ra = 21078$.

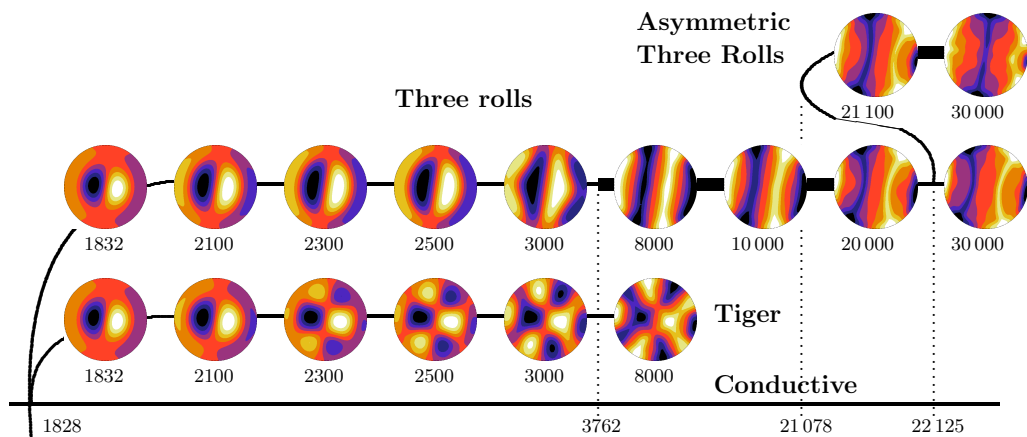


FIG. 14: (Color online) Schematic bifurcation diagram of branches emanating from $m = 1$ instability. Two branches bifurcate simultaneously at $Ra = 1828$. Near the bifurcation, states along both branches have the form of a dipole. States along one branch evolve into a **Three-roll** state, while along the other branch evolve to a form called **Tiger**. The three-roll state is stable for $3762 \leq Ra \leq 20393$, and the tiger branch is never stable. The **Asymmetric Three-Roll** branch is formed at $Ra = 22125$, via a subcritical pitchfork bifurcation from the three-roll branch, reversing direction at a saddle-node bifurcation at $Ra = 21078$.

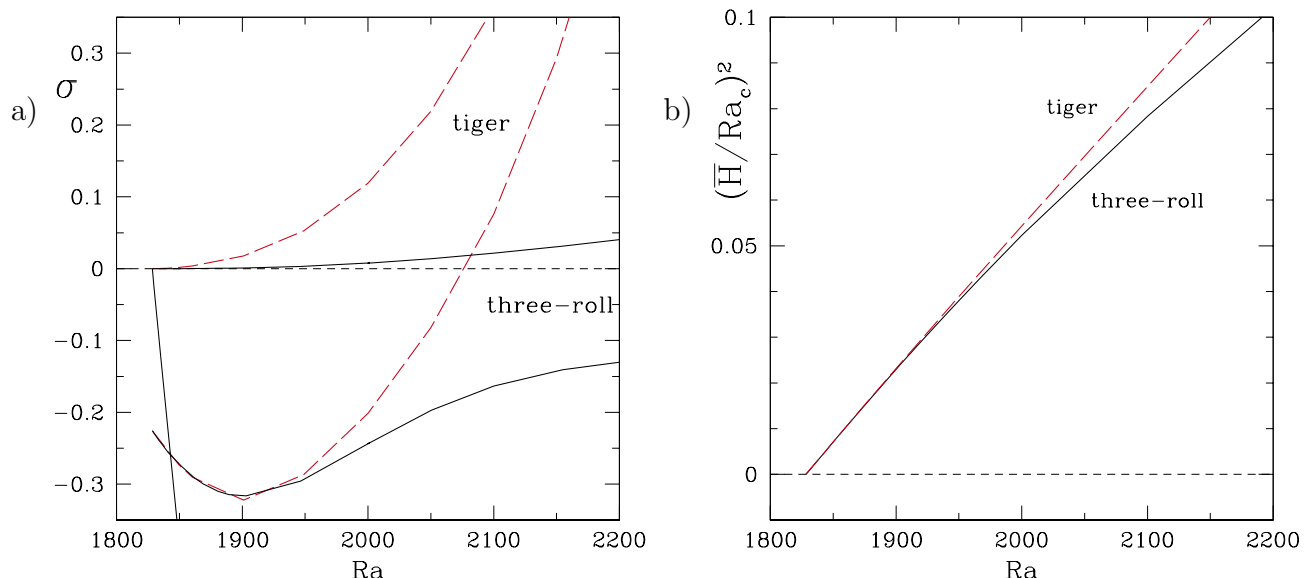


FIG. 15: (Color online) a) Leading eigenvalues of the tiger (long-dashed, brick) and three-roll (solid, black) branches. The eigenvalues of the tiger branch grow rapidly as Ra increases, while the three-roll branch is weakly unstable until $Ra = 3762$. The rapidly decreasing eigenvalue is that associated with the formation of these branches. b) The tiger and three-roll branches have the same curvature near onset.

unstable immediately after it forms. At the same time, the three-roll branch also becomes weakly unstable, though it eventually stabilizes at $Ra = 3762$. Instability near onset is another unexpected feature of these branches. The three-roll branch becomes unstable again at $Ra = 20\,393$, as shown in figure 16.

We have sought to better understand the primary $m = 1$ bifurcation, at which both the tiger and three-roll branches bifurcate simultaneously. First, we have verified that the three-roll and the tiger branches are distinct by following them around the pitchfork bifurcation, producing symmetrically-related branches. Thus the possibility that our continuation procedure has jumped from one branch to another is ruled out. Figure 15b shows that both the tiger and the three-roll branches emerge via a pitchfork bifurcation, i.e. that $\bar{H} \propto \sqrt{Ra - Ra_c}$, or, equivalently, that

$$\left(\frac{\bar{H}}{Ra_c}\right)^2 = \alpha \frac{Ra - Ra_c}{Ra_c} \quad (32)$$

for $Ra_c = 1828.37 \leq Ra \lesssim 1900$. Figure 15b also shows that the constant of proportionality in (32) is the same for both branches ($\alpha \approx 0.59$). Thus the two branches initially share not only a vertical tangent, but even the same curvature.

Simultaneously bifurcating and non-equivalent branches are encountered in a number of situations, notably pitchfork bifurcation in the presence of D_4 symmetry, such as in a square box [14, 15]. In the D_4 case, one set of branches contains solutions whose axes of symmetry are the vertical or the horizontal midline of the square, while, for the other set of solutions, the symmetry axes are the diagonals. Although the two types of branches bifurcate simultaneously, they are not related to one another by a symmetry operation of D_4 , and so are not dynamically equivalent. For $O(2)$, in contrast to D_4 , the concepts of vertical, horizontal and diagonal have no meaning: solutions of any orientation can be obtained by rotation, and so must all be dynamically equivalent. An explanation of the $m = 1$ behavior is the subject of a separate investigation.

Most of the results given above are consistent with the time-dependent simulations of our companion paper [3, 4], summarized in figure 1. The inconsistencies can largely be explained as a consequence of finite integration time and very weak instability. This accounts for the observation of a symmetric three-roll state for $25\,000 \leq Ra \leq 30\,000$, a range over which it is unstable, rather than its stable asymmetric counterpart. The same is true of the long-lived dipole state observed near onset at $Ra = 2000$. In all of these cases, the largest eigenvalue is less than 0.5, which would not have allowed initially small perturbations to grow to appreciable levels over the duration of our time-dependent simulations; this is true for all of the steady states shown in figure 1 summarizing the time-dependent simulations.

Time-dependent simulation from an initial dipole state at various Rayleigh numbers also yielded various interesting transients [3, 4], and led to the discovery of an oscillatory pattern, the rotating S, and of two new steady patterns: the dipole smile, whose branch we have not continued, and the CO, described in the next section.

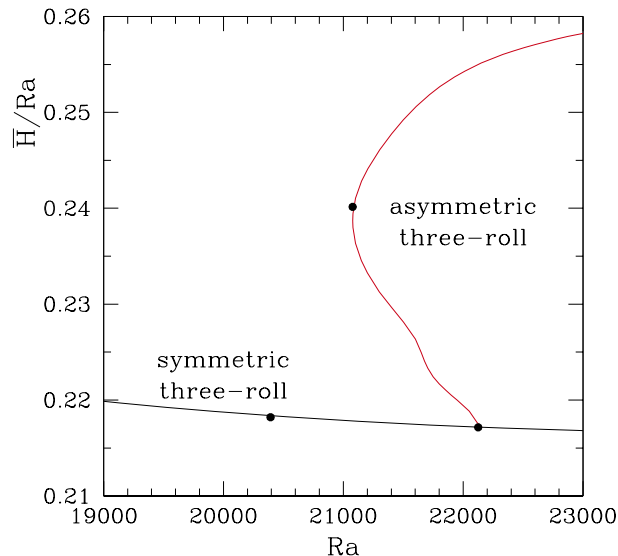


FIG. 16: (Color online) Enlargement of bifurcation diagram of figure 13. The symmetric three-roll branch loses stability at $Ra = 20393$. A subcritical bifurcation at $Ra = 22125$ from the symmetric three-roll branch leads to the creation of the asymmetric three-roll branch, which is stabilized by a saddle-node bifurcation at $Ra = 21078$.

G. Two-roll and CO branches

Finally, we mention another set of branches which, like the one-torus branches, appear to be unconnected to the conductive state. These are the **Two-roll** and the **CO branch**, shown in figures 17 and 18.

Figure 1 shows how these branches were originally found by time-integration, starting from quasi-steady states at $Ra = 2000$. A CO state was found by starting from a dipole and setting $Ra = 10000$ and a two-roll state by starting from a pizza and setting $Ra = 16000$. The two-roll branch originates at a saddle-node bifurcation at $Ra = 8677$, where it is connected to an unstable branch containing states which also have two rolls. Figure 18 shows that, for high Ra , states on the stable branch have an indentation in the central boundary which divides the rolls, while those on the unstable branch have a protrusion. Two-roll states have also been observed in the numerical simulations at $Ra = 14200$ by Ma *et al.* [7] and at $Ra = 37500$ by Leong [6]. The two-roll branches are very robust: both exist at least until $Ra = 30000$ and the upper branch is stable for $Ra \leq 28086$. We have been able to compute the CO branch only for $7167 \leq Ra \leq 10348$, and it is stable for $Ra \leq 10087$. The two-roll states have two symmetry axes (i.e. D_2), while the CO states, containing two light regions, one curved and one oval) have only one symmetry axis (Z_2).

Figure 19 shows that the high Rayleigh number ($Ra \geq 20000$) asymmetric three-roll states and four-roll states greatly resemble two-roll states. Along all of the branches, the convective structures widen as Ra increases for all the branches: this is the form taken in this confined geometry of the well-known increase in wavelength for large systems of parallel rolls. For the branches emerging from the $m = 1$ and $m = 2$ primary bifurcations, this tendency eventually leads, after secondary bifurcations and more gradual deformations, to states which primarily contain two rolls. These are far removed from the trigonometric forms of the dipole and pizza states that prevail along these branches at low Ra .

V. CONCLUSION

We have presented an intricate bifurcation diagram describing Rayleigh-Bénard convection in a cylinder with aspect ratio $\Gamma = 2$ and $Pr = 6.7$ for $Ra \leq 30000$. This study is complementary to the time-dependent simulations described in our companion paper [4]; the branches of the bifurcation diagram were obtained by continuation from the stable states resulting from time integration. We have determined the bifurcation-theoretic origin of these states, including the five states observed experimentally by Hof *et al.* In one case, the path is straightforward: the four-roll branch results from a secondary bifurcation from the pizza branch, which in turn arises from a primary $m = 2$ bifurcation

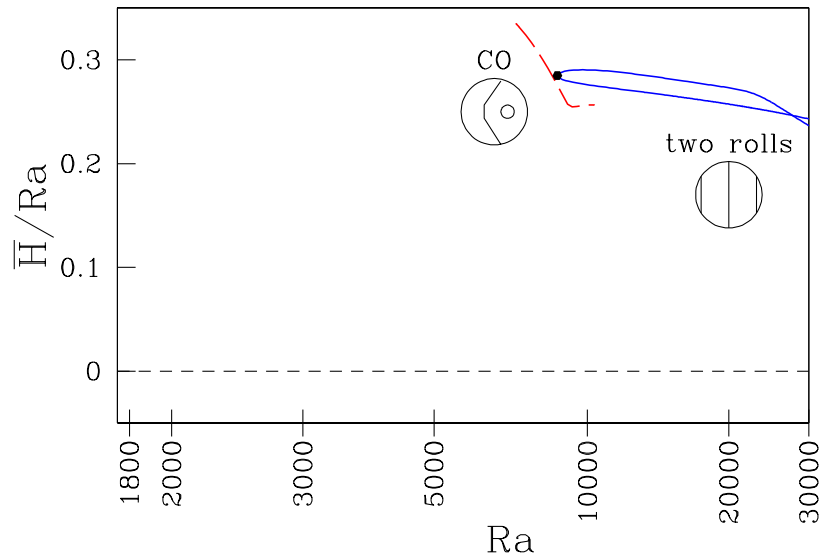


FIG. 17: (Color online) Partial bifurcation diagram containing the two-roll and CO branches. Two-roll branches (solid, blue) arise via saddle-node bifurcation at $Ra = 8677$. CO branch (dashed, red) has been computed for $7167 \leq Ra \leq 10348$. The apparent intersections (between the two-roll and CO branches and between the stable and unstable two-roll branches) is an artifact of the projection.

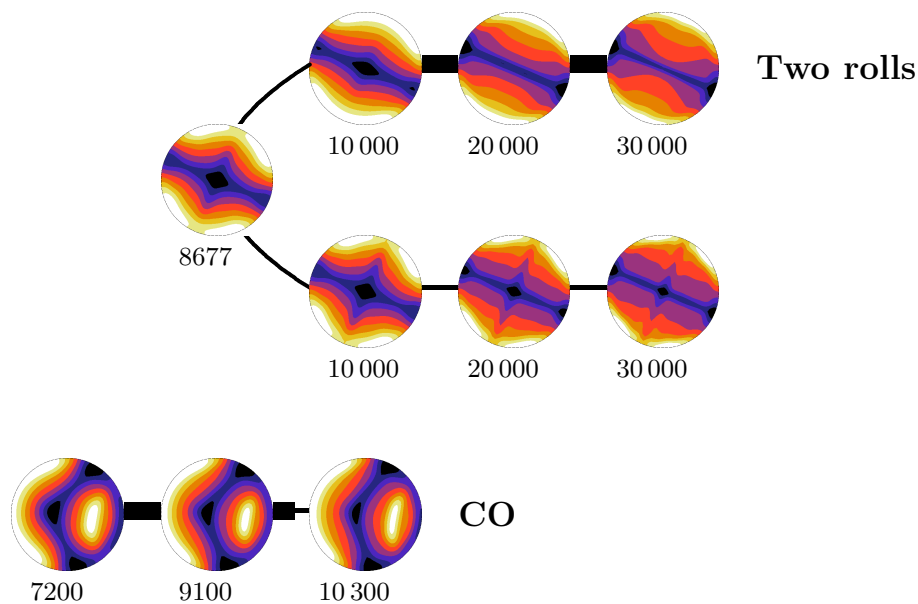


FIG. 18: (Color online) Schematic partial bifurcation diagram showing the two-roll and CO branches. The two-roll branches originate at a turning point at $Ra = 8677$ and have been computed for $Ra \leq 30000$. The upper branch is stable for $Ra \leq 28086$. The CO branch has been calculated in the range $7167 \leq Ra \leq 10348$; it is stable for $Ra \leq 10087$.

from the conductive branch. In another case, it is more tortuous: for $m = 3$, two additional saddle-node bifurcations must be traversed between the primary marigold branch and the stable Mercedes branch which is actually observed. The torus and two-roll branches turned out to be disconnected (as far as we can tell) to the conductive state. Finally,

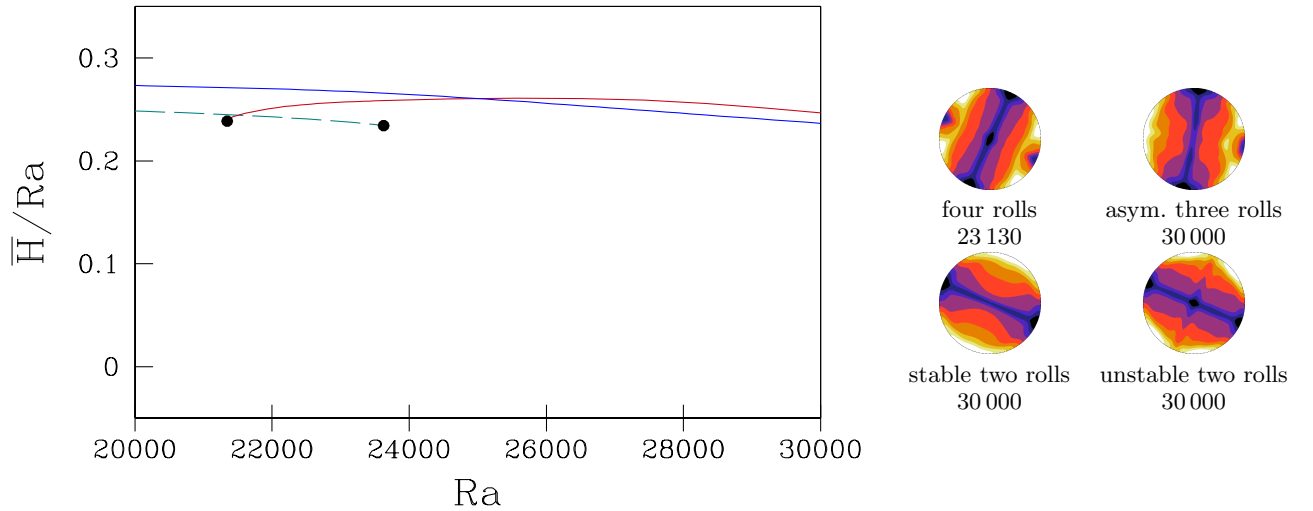


FIG. 19: (Color online) Four-roll (dashed, turquoise), asymmetric three-roll (solid, brick) and two-roll branches (solid, blue) at high Ra .

we have located the primary $m = 1$ bifurcation leading to the three-roll branch, but it is accompanied by another simultaneously bifurcating branch and has unexpected stability properties. We have also traced the disconnected CO branch and the two-torus branch arising from a primary $m = 0$ bifurcation. A schematic version of the bifurcation diagram is given in figure 20, while tables II and III list all of the branches we have obtained, as well as the bifurcations and their nature.

The diagram we have obtained contains 17 branches of steady states, but is nonetheless incomplete. Although we have followed the primary branches originating at 5 bifurcations along the conductive branch, there are literally hundreds of other primary bifurcation points in the range $Ra \leq 30\,000$. Each of the primary branches thus engendered can and does undergo many secondary bifurcations. In addition, while calculating the stability of the various branches we have observed many eigenvalues cross zero, signalling the appearance of a new branch. Finally, there is no way to ascertain how many other disconnected branches. It is surely unfeasible and unproductive to strive to find all branches.

Despite the complexity of the bifurcation diagram, its main features can be described quite simply. Circle pitchfork bifurcations to trigonometric branches dictated by the geometry – dipole, pizza, marigold, two-torus – take place at low Rayleigh numbers. These undergo various secondary bifurcations at intermediate Rayleigh numbers that lead to states with rolls. At high Rayleigh numbers, there are three types of stable branches: torus, Mercedes, and states essentially containing two rolls.

Our goal of relating the states obtained by time integration to the bifurcation diagram is largely realized, but there remain a few loose ends. One is to complete our understanding of the two simultaneously bifurcating $m = 1$ branches. Another small and clear-cut goal is to incorporate the time-periodic rotating S state we have described in [3, 4] into the bifurcation diagram by ascertaining its bifurcation-theoretic origin and exact domain of existence and stability. Comparing our study to that of Ma *et al.*, we find very similar values for the five primary pitchfork bifurcations, for the secondary pitchfork bifurcation creating the four-roll branch, and for the two secondary pitchfork bifurcations which stabilize the two-torus branch. The other bifurcations in Table III are not present in Ma *et al.*. These authors did, however, compute an additional stable four-spoked pattern at $Ra = 14\,200$, whose bifurcation-theoretic genesis could be interesting to determine.

Our study also points in several larger directions. It would be desirable to incorporate improved versions of the numerical methods we have used, namely adjustment of Ra within the Newton iteration, the inverse Arnoldi method, and the calculation of traveling waves as steady states in a rotating frame. This example could also be used as a test case to try to understand and to control the enormous variability in performance of BiCGSTAB in solving the linear equations of Newton’s method in different regions of the bifurcation diagram. Finally, an extensive but straightforward goal is to compute a bifurcation diagram for the case in which the sidewalls are thermally conducting rather than insulating. Time-dependent simulations have already yielded initial conditions and approximate stability ranges for many branches [3, 4]. For the conducting case, as for the insulating case, construction of a complete bifurcation diagram is doubtless impossible, but the stable steady and time-periodic states could all be traced back to their bifurcation-theoretic origin from the conductive state as we have done here.

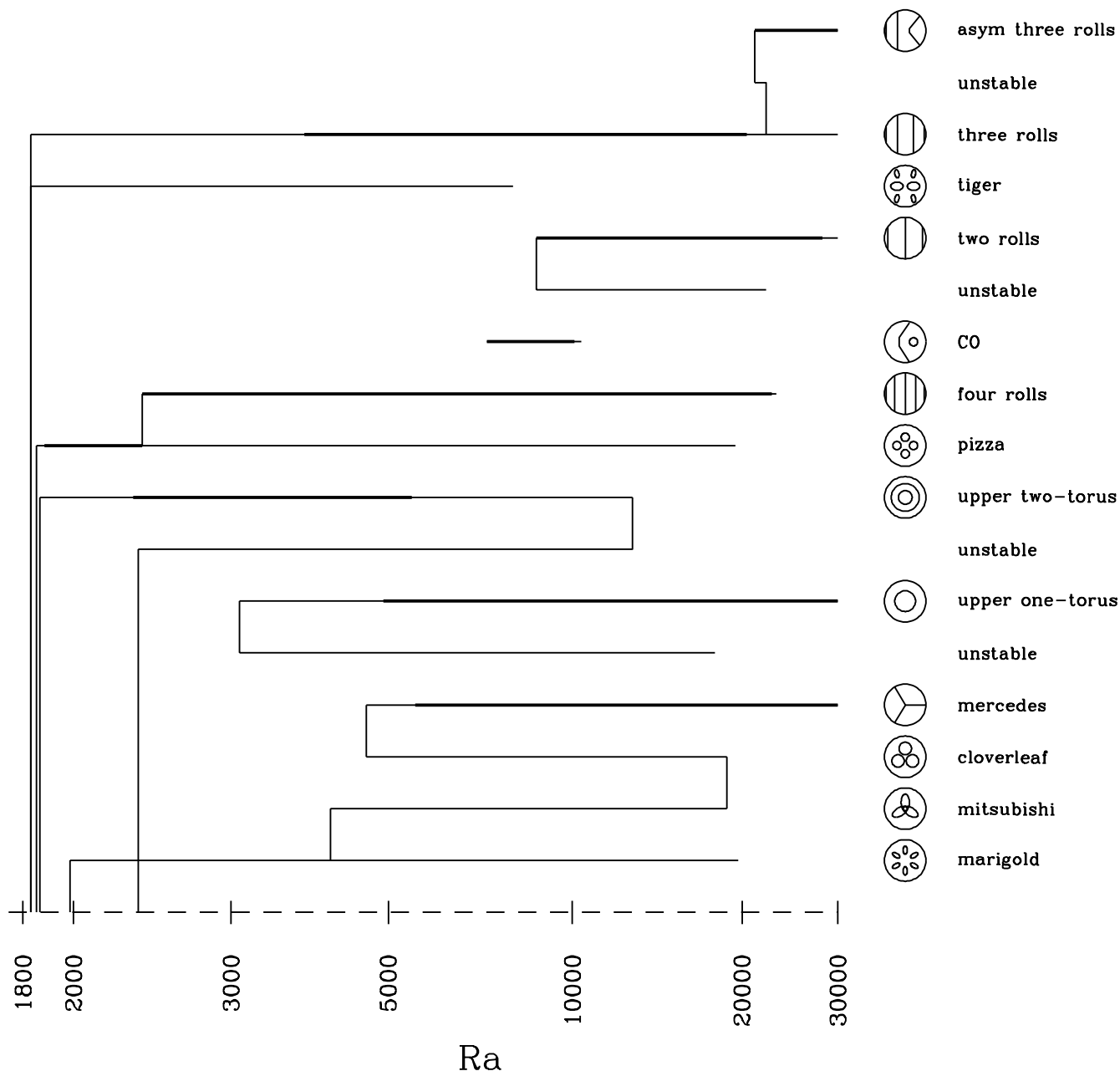


FIG. 20: Schematic bifurcation diagram. Arbitrary quantity of the vertical axis chosen to eliminate all but one intersection. Bold lines indicate stable portions of branches.

The complexity of the bifurcation diagram we have computed is interesting in light of the recent computational discovery of large numbers of unstable solutions of wall-bounded shear flows, e.g. [16]. It is hypothesized that weak turbulence can be understood as chaotic trajectories, e.g. [17], that visit in turn the vicinities of the various unstable branches, which are created at saddle-node bifurcations. Our study contributes two observations to this line of research. First, this example provides a reminder that the existence of a large number of unstable solutions is a typical property of the hydrodynamic equations. Second, our study underlines the fact that such multiplicity can occur in the absence of complicated dynamics.

This study showcases our numerical methods for carrying out time-integration, branch continuation and linear stability analysis by using a single code with several different high-level drivers. Newton's method has many advantages: it is much faster and much more precise, and can compute unstable states. Time integration remains, nevertheless,

absolutely essential for generating initial states, especially since several important branches are disconnected from the conductive state. Although our cylindrical Rayleigh-Bénard computation is quite specific, it demonstrates what can be accomplished for three-dimensional nonlinear problems by combining matrix-free preconditioned numerical methods with dynamical systems theory.









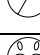





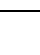
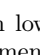
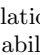
family	branch		Ra_{\min}		Ra_{\max}	
			existence	stability	stability	existence
2	pizza		1849.4	1879	2353	19 450
	four-roll		2353	2353	22 660	23 130
0	upper two-torus		1861.6	2300	5438	12 711
	lower two-torus		2328.0	--	--	12 711
	upper one-torus		3076.4	4918	$\geq 30\ 000$	$\geq 30\ 000$
	lower one-torus		3076.4	--	--	$\geq 17\ 857$
3	marigold		1985.3	--	--	$\geq 19\ 695$
	mitsubishi		4103	--	--	18 762
	cloverleaf		4634.2	--	--	18 762
	mercedes		4634.2	5503	$\geq 30\ 000$	$\geq 30\ 000$
1	tiger		1828.4	--	--	≥ 7936
	three-roll		1828.4	3762	20 393	$\geq 30\ 000$
	upper asymmetric three-roll		21 077.7	21 078	$\geq 30\ 000$	$\geq 30\ 000$
	lower asymmetric three-roll		21 077.7	--	--	22 125
other	upper two-roll		8677.0	8677	28 086	$\geq 30\ 000$
	lower two-roll		8677.0	--	--	$\geq 30\ 000$
	CO		≤ 7167	≤ 7167	10 087	$\geq 10\ 348$

TABLE II: List of all convective branches computed, with lower and upper limits of existence and stability. Stable patterns (between limits in boldface) should be observable in experiments or time-dependent simulations. Inequalities (\geq or \leq) indicate a lower or upper bound for the corresponding Ra : calculation of the branch either terminated for an unknown reason, or continued past 30 000. Dashes (--) indicate the lack of stability limits for branches which are unstable throughout.

Acknowledgments

We thank Tom Mullin and Björn Hof for their continued interest in this work. We thank Dwight Barkley, Edgar Knobloch, Laurent Martin-Witkowski, Paul Matthews, and Isabel Mercader for useful discussions. All of the computations were performed on the computers of IDRIS (Institut pour le Développement des Ressources Informatiques et Scientifiques) of CNRS (Centre National pour la Recherche Scientifique) under project 1119.

family	bifurcation	Ra	comments
2	circle pitchfork	1849.4	creates pizza branch
	pitchfork	2353	creates four-roll branch
	eigenvalue crossing	1879	stabilizes pizza branch
	turning point	19 450	terminates pizza branch
	eigenvalue crossing	22 660	destabilizes four-roll branch
	turning point	23 060	terminates four-roll branch
0	pitchfork	1861.6	creates upper two-tori branch
	pitchfork	2328.0	creates lower two-tori branch
	turning point	12 711	terminates upper and lower two-tori branches
	eigenvalue crossing	2116	stabilizes upper two-tori branch against $m = 2$ eigenvector
	eigenvalue crossing	2300	stabilizes upper two-tori branch against $m = 1$ eigenvector
	eigenvalue crossing	5438	destabilizes upper two-tori branch against $m = 1$ eigenvector
0	turning point	3076.4	creates upper and lower one-torus branches
	eigenvalue crossing	3330	stabilizes upper one-torus branch against $m = 6$ eigenvector
	eigenvalue crossing	3438	stabilizes upper one-torus branch against $m = 2$ eigenvector
	eigenvalue crossing	4408	stabilizes upper one-torus branch against $m = 5$ eigenvector
	eigenvalue crossing	4582	stabilizes upper one-torus branch against $m = 3$ eigenvector
	eigenvalue crossing	4918	stabilizes upper one-torus branch against $m = 4$ eigenvector
3	circle pitchfork	1985.3	creates marigold branch
	pitchfork	4103	creates mitsubishi branch
	turning point	4634.2	creates mercedes and cloverleaf branches
	turning point	18 762	terminates cloverleaf and mitsubishi branches
	eigenvalue crossing	5503	stabilizes mercedes branch
1	circle pitchfork	1828.4	creates tiger and three-roll branches
	eigenvalue crossing	3762	stabilizes three-roll branch
	eigenvalue crossing	20 393	destabilizes three-roll branch
	turning point	21 077.7	creates asymmetric three-roll branch
	subcritical pitchfork	22 125	terminates asymmetric three-roll branch
other	turning point	8677.0	creates two-roll branches
	eigenvalue crossing	28 086	destabilizes two-roll branch
	eigenvalue crossing	10 087	stabilizes CO branch

TABLE III: List of all bifurcations located. Circle pitchfork bifurcation breaks axisymmetry, creating “circle” of new states parametrized by azimuthal phase. Pitchfork bifurcation breaks a reflection symmetry, creating two branches. Eigenvalue crossings are necessarily accompanied by bifurcations, whose nature we have not investigated. Comments such as “stabilizes”, “destabilizes”, “creates”, “terminates” are to be interpreted in the direction of increasing Rayleigh number.

-
- [1] B. Hof, G.J. Lucas & T. Mullin, *Flow state multiplicity in convection*, Phys. Fluids **11**, 2815–2817 (1999).
- [2] B. Hof, *The visualisation of convective flow patterns in water in tilted cells with variable geometry*, Master’s thesis, University of Manchester, 1997.
- [3] K. Borońska, *Motifs tridimensionnels dans la convection de Rayleigh-Bénard cylindrique*, Thèse de doctorat, Université de Paris 7, 2005.
- [4] K. Borońska & L.S. Tuckerman, *Extreme multiplicity in cylindrical Rayleigh-Bénard convection, I. Time-dependence and oscillations*, Phys. Rev. E, submitted.
- [5] T.B. Benjamin & T. Mullin, *Notes on the multiplicity of flows in the Taylor experiment*, J. Fluid Mech. **121**, 219–230 (1982).
- [6] S.S. Leong, *Numerical study of Rayleigh-Bénard convection in a cylinder*, Numerical Heat Transfer, Part A **41**, 673–683 (2002).
- [7] D.J. Ma, D.J. Sun & X.Y. Yin, *Multiplicity of steady states in cylindrical Rayleigh-Bénard convection*, Phys. Rev. E **74**, 03 7302 (2006).
- [8] C.K. Mamun & L.S. Tuckerman, *Asymmetry and Hopf bifurcation in spherical Couette flow*, Phys. Fluids **7**, 80–91 (1995).
- [9] L.S. Tuckerman & D. Barkley, *Bifurcation analysis for time-steppers*, in Numerical Methods for Bifurcation Problems and Large-Scale Dynamical Systems, ed. by E. Doedel & L.S. Tuckerman (Springer, New York, 2000), p. 452–466.
- [10] H.A. van der Vorst, *Bi-CGSTAB: A fast and smoothly converging variant of Bi-CG for the solution of nonsymmetric linear systems*, SIAM J. Sci. Stat. Comput. **13**, 631 (1992).
- [11] W.E. Arnoldi, *The principle of minimized iterations in the solution of the matrix eigenvalue problem*, Q. Appl. Math **9**, 17 (1951).
- [12] S. Xin, P. Le Quééré & L.S. Tuckerman, *Bifurcation analysis of double-diffusive convection with opposing horizontal thermal and solutal gradients*, Phys. Fluids. **10**, 850–858 (1998).
- [13] L. Martin-Witkowski, private communication.
- [14] J.D. Crawford, E. Knobloch, *Symmetry and symmetry-breaking bifurcations in fluid dynamics*, Annu. Rev. Fluid Mech. **23** 341 (1991).
- [15] A. Bergeon, D. Henry & E. Knobloch, *Three-dimensional Marangoni-Benard flows in square and nearly-square containers*, Phys. Fluids **13**, 92–98 (2001).
- [16] B. Hof, C.W.H. van Doorne, J. Westerweel, F.T.M. Nieuwstadt, H. Faisst, B. Eckhardt, H. Wedin, R.R. Kerswell, F. Waleffe, *Experimental Observation of Nonlinear Traveling Waves in Turbulent Pipe Flow*, Science **305**, 1594–1598 (2004).
- [17] J. F. Gibson, J. Halcrow, P. Cvitanović, *Visualizing the geometry of state space in plane Couette flow*, J. Fluid Mech. **611**, 107–130 (2008).